Enhancement of immiscible two-phase displacement flow by introducing nanoparticles and employing electro- and magneto-hydrodynamics

Morteza Esmaeilpour *, Maziar Gholami Korzani

Department of Civil Engineering, Geo and Environmental Sciences, Karlsruhe Institute of Technology, 76131 Kralsruhe, Germany

ARTICLE INFO

Keywords:
Lattice Boltzmann method
He-chen-zhang method
Non-Newtonian fluid displacement
Magneto-hydrodynamics
Electro-hydrodynamics
Nanoparticles

ABSTRACT

In this study, two-component displacement of a time-dependent non-Newtonian fluid by a Newtonian fluid in a two-dimensional inclined channel is simulated. Using a special multi-component model of the lattice Boltzmann method that is called He-Chen-Zhang, made it possible to do the simulations for non-uniform density and very high viscosity ratios. The main focus of this study is altering the flow pattern and displacement efficiency by Applying Electro- and magneto-hydrodynamic fields, using added nanoparticles and heating the channel walls. Displacement efficiency in different cross-sections, thickness of the static wall layer at the top and bottom of the channel, development of interfacial instabilities, magnitude of generated forces and, temperature distribution in the simulation environment are analyzed comprehensively to fully control the fingering structure. Investigation of injected fluid movement in the other one and displacement efficiency showed that enhancement in the power of the electric field is associated with displacement efficiency alteration in various longitudinal sections of the channel. However, removing the residual layer at the top and bottom of the fingering structure doesn't cause the total efficiency of displacement (M_t) to change significantly since the axial motion of the invading fluid is weakened. In contrast, applying magnetic field, increasing the Hartmann number and changing the rotation angle of the coordinate system (to 180), enhances the axial velocity and displacing ability of this fluid. Furthermore, for $Ha = 10$ and $\theta = 0$, with the transverse velocity rising, displacement efficiency for longitudinal sections close to the channel axis decreases and the occurrence of interfacial instabilities is inevitable.

Credit author statement

Morteza Esmaeilpour, Programming, implementation of the computer code supporting algorithms, Validation, Writing - original draft preparation, Visualization, Investigation. Maziar Gholami Korzani, Supervision, Writing-reviewing editing

1. Introduction

Transport of crude oil in pipe-lines (Taghavi et al., 2012), oil recovery (Abedi et al., 2012; Abedi and Kharrat, 2016) food processing, and coating are industrial examples of pressure or gravitational driven displacement flow. In these cases, high viscosity of materials creates a flow which is in the laminar range. However, it is still difficult to model fluid-fluid interface in immiscible flows even by considering laminarity. Therefore, precision of numerical models and schemes, which are capable of capturing dynamics of the interface and computationally efficient, are of great significance (Heidaryan, 2019).

Penetration of a fluid with a low viscosity into a fluid with a higher viscosity results in a two-layer or two-core annular flow leading to the occurrence of interfacial instabilities, such as the Kelvin-Helmholtz. The dynamics of these flows can be simulated in miscible (Etrati and Frigaard, 2018; Mishra et al., 2012; Sharma et al., 2020) and immiscible (Patmonoaji et al., 2020; Suo et al., 2020; Tsuzuki et al., 2019) states. Accordingly, roll-up structures occur in miscible displacements (Bischofberger et al., 2014; Shabouei and Nakshatrala, 2020), and sawtooth structures occur in immiscible displacements (Redapangu et al., 2012). (Goyal and Meiburg, 2006) numerically studied miscible displacements of highly viscous fluids, and they observed that, two-dimensional instabilities (caused by the shear stress between the two fluids) turn into three-dimensional instabilities by increasing the applied flow rate. This observation is completely consistent with laboratory findings by (Petitjeans and Maxworthy, 1996) and theoretical solutions provided by (Lajeunesse et al., 1999). In the field of oil recovery (Taghavi et al, 2009, 2011), numerically and experimentally investigated the displacement of two miscible fluids, and similar instabilities at low applied velocities in

* Corresponding author.
E-mail addresses: morteza.esmaeilpour@kit.edu (M. Esmaeilpour), m.gholami@kit.edu (M. Gholami Korzani).

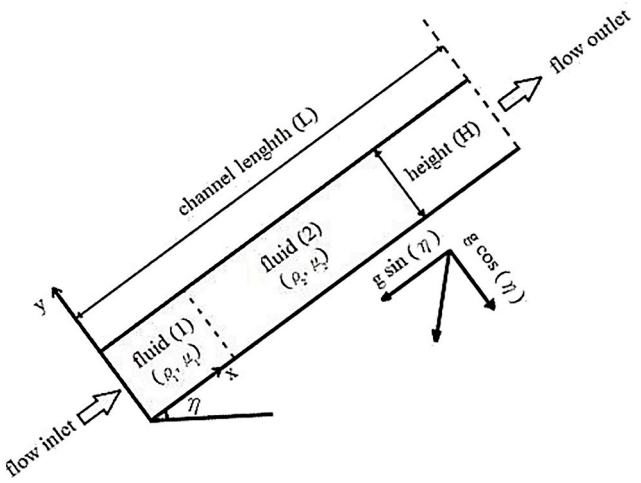

Fig. 1. A schematic showing the initial geometry (without observing the proportionality) and structure of the flow. The inlet and outlet of the channel are located at x = 0 and x = L, respectively. The length to height ratio of the channel is L/H = 30. In the initial state, the channel is filled with fluids 1 and 2 at $0 \leq x \leq 5$ and $5 \leq x \leq L$, respectively.

exchange flows were observed (Sahu et al., 2009a). analyzed the effects of gradient angles and the Froude number on miscible flows considering nonequality of densities and viscosities. The presence of tiny instabilities is consistent with their previous findings regarding the linear stability analysis (Sahu et al., 2009b). (Yang and Yortsos, 1997) investigated miscible displacements in Stokes flows between parallel plates. The results of their studies shows that fingering instabilities increases by increasing viscosity ratio. Nevertheless, displacement efficiency in different cross-sections and thickness of the static wall layer are rarely addressed in the literature. Therefore, a comprehensive investigation of static wall layer alteration due to these instabilities seems to be necessary considering the enormous effects of interfacial instabilities on the displacement efficiency.

There are few studies investigating the displacement of non-Newtonian fluids by Newtonian fluids (Dimakopoulos and Tsamopoulos, 2003). investigated the displacement of viscoplastic fluids by air in convergent channels. They illustrated that some parts of the displaced fluid were left unyielded at the corners of the channel (Papaioannou et al., 2009). investigated the displacement of air by viscoplastic fluids, and they introduced conditions for the separation of the injected fluid from channel walls (Ebrahimi et al., 2016). as well as (Wielage-Burchard and Frigaard, 2011) studied the displacement of Bingham fluids by other fluids (at equal densities), and investigated the thickness of the static layer left on walls for different Bingham numbers (Frigaard and Nouar, 2005). studied impacts of viscosity adjustment criteria on dynamics of flow including Simple (Allouche et al., 2000), Bercovier-Engleman (Mitsoulis and Tsamopoulos, 2017), and Papanastasiou (Khan and Sultan, 2018) models. According to their findings, the Papanastasiou model performed better than the rest models. Unfortunately, displacement of time-dependent non-Newtonian fluids (like hydrogenated castor oil, xanthan gum solutions and aqueous iron oxide gels) by Newtonian ones and effects of wall temperature have not been yet addressed. Furthermore, simplified models of fluid motion were employed to study the aforementioned problems leading to lower accuracy and less reliability of results.

Several researchers declared that Lattice Boltzmann method is a trustworthy scheme for modeling fluid flows and transfer theories in recent years. Various approaches of this method are available among which we can mainly refer to the color gradient (Akai et al., 2018), the Shan-Chen (Baakeem et al., 2020), the free energy (Mino and Shinto, 2020), and the He-Chen-Zhang (Sudhakar and Das, 2020). Many scientists applied the Shan-Chen model to simulate immiscible (Chin, 2002), but due to very low Reynolds numbers used in these studies, they didn't observe any sign of interfacial instabilities (Redapangu et al., 2012). investigated a displacement flow for two immiscible Newtonian fluids at medium Reynolds numbers using the He-Chen-Zhang (Zhang et al., 2000) method, and effects of Atwood number, gradient angles, and viscosity ratios on flow dynamics were studied. Their results shows that sawtooth-structure instabilities occur at the interface of the two fluids for this type of displacements. Similar studies, in which impacts of yield stress on the displacement efficiency evaluated, were conducted by Vikhansky (Vikhansky, 2008, 2012) and Derksen (2013) on viscoplastic fluids. Significant advantages of the lattice Boltzmann method over other numerical methods like Smoothed Particle Hydrodynamics (Gholami Korzani et al, 2014, 2016, 2017; Rahmat et al., 2019) made it an appropriate scheme for modeling these problems. These advantages include Auto-separation of phases, computational efficiency, simplicity of coding, and local calculation of shear rates (Sadeghi et al., 2018; Sadeghi and Shadloo, 2017; Safdari Shadloo, 2019).

The above-mentioned studies concerning displacement flow and fingering mainly concentrated on the impacts of dimensionless numbers and viscosity criterion on dynamics of flow without offering any practical solutions to increase the displacement efficiency utilizing external forces. In this paper, we propose a new approach by adding nano-particles to the injected fluid for employing electro-hydrodynamic and magneto-hydrodynamic fields as applied external forces, and then the impacts of nano-particles and other external forces, such as thermal fields, on the displacement of time-dependent non-Newtonian fluids by Newtonian fluids are analyzed.

In this manuscript, after introducing boundary conditions and the equations governing the fluid flow, a simple example of displacement flow in a tilted channel is simulated. Then, the results of this simulation are compared with the results of the study conducted by (Redapangu et al., 2012). Moreover, a mesh sensitivity analyses was carried out. Finally, the results of the simulations are discussed and interpreted by presenting two groups of figures which are used to exhibit the displacement efficiency and the appearance of flow. These figures show the efficiency of displacement in all longitudinal and cross-sections of the channel, the amount of displaced fluid left in the channel, the thickness of the static layer at the top and bottom of the channel, development of instabilities, and placement pattern of two fluids in the channel.

2. Numerical modeling

Consider a two-dimensional inclined channel which is initially filled with a stagnant incompressible Newtonian fluid with a viscosity of μ_2 and density of ρ_2 (fluid 2). This fluid is displaced in an immiscible manner due to the presence of a flow applied by a fluid with a viscosity of μ_1 and density of ρ_1 (fluid 1). The inlet and outlet of the channel are located at x 0 and x L, and its walls at y 0 and y H.

We used the hydrodynamic boundary condition for the upper and lower walls of the channel, a fully developed velocity profile at the inlet, and the Neumann boundary condition for pressure at the outlet (through extrapolation). We also considered the height-to-length ratio of the channel to be 1 to 30 in all the simulations, and the inclination angle of the channel was considered according to the longitudinal axis. Fig. 1 shows a schematic of the above conditions.

2.1. Numerical method

The present study is based on a model of the He and Chen's method (He et al., 1999a, 1999b) developed by Sahu and Vanka (2011) for fluids with unequal viscosities. In what follows, we briefly describe this model.

The two distribution functions f and g are defined using relations (1) and (2) in the collision step:

$$f_\alpha(x+e_\alpha\delta t,t+\delta t) \quad f_\alpha(x,t) \quad \frac{f_\alpha(x,t) \quad f_\alpha^{eq}(x,t)}{\tau} + \frac{2\tau \quad 1}{2\tau}\frac{(e_\alpha \quad u)\cdot\nabla\psi(\phi)}{c_s^2}\Gamma_\alpha(u)\delta t \tag{1}$$

$$g_\alpha(x+e_\alpha\delta t,t+\delta t) \quad g_\alpha(x,t) \quad \frac{g_\alpha(x,t) \quad g_\alpha^{eq}(x,t)}{\tau}\frac{2\tau \quad 1}{2\tau}(e_\alpha \quad u) \cdot\left[\Gamma_\alpha(u)(F_s+G) \quad (\Gamma_\alpha(u) \quad \Gamma_\alpha(0))\nabla\left(P \quad \rho c_s^2\right)\right] \tag{2}$$

where

$$\Gamma_\alpha(u) \quad t_\alpha\left[1+\frac{e_\alpha\cdot u}{c_s^2}+\frac{(e_\alpha\cdot u)^2 \quad u^2}{2c_s^4 \quad 2c_s^2}\right] \tag{3}$$

In the above equations, u represents the velocity vector, and τ is the relaxation time, which is related to the kinematic viscosity through the relation $\gamma \quad (\tau \quad 0.5)c_s^2\delta$. Also, c_s is the speed of sound, and its value is set to 0.333 in the above equation. We use Relation (4) to find the mesoscopic velocity at the lattice scale:

$$e_\alpha \quad \begin{cases} (0,0)\leftarrow\alpha \quad 0 \\ \left[\cos(\alpha \quad 1)\frac{\pi}{2},\sin(\alpha \quad 1)\frac{\pi}{2}\right]\leftarrow\alpha \quad 1,2,3,4 \\ \sqrt{2}\left[\cos\left(\frac{(\alpha \quad 5)\pi}{2}+\frac{\pi}{4}\right),\sin\left(\frac{(\alpha \quad 5)\pi}{2}+\frac{\pi}{4}\right)\right]\leftarrow\alpha \quad 5,6,7,8 \end{cases} \tag{4}$$

As for the weight functions, we have the following:

$$t_\alpha \quad \begin{cases} \frac{4}{9}\leftarrow\alpha \quad 0 \\ \frac{1}{9}\leftarrow\alpha \quad 1,2,3,4 \\ \frac{1}{36}\leftarrow\alpha \quad 5,6,7,8 \end{cases} \tag{5}$$

In addition, the equilibrium distribution functions are obtained from equations (6) and (7):

$$f_\alpha^{eq}(u) \quad t_\alpha\phi\left[1+\frac{e_\alpha\cdot u}{c_s^2}+\frac{(e_\alpha\cdot u)^2 \quad u^2}{2c_s^4 \quad 2c_s^2}\right] \tag{6}$$

$$g_\alpha^{eq}(u) \quad t_\alpha\left[P+\rho c_s^2\left(\frac{e_\alpha\cdot u}{c_s^2}+\frac{(e_\alpha\cdot u)^2 \quad u^2}{2c_s^4 \quad 2c_s^2}\right)\right] \tag{7}$$

The index function(ϕ), pressure (P), and velocity (u) are calculated using relations (8) to (10):

$$\phi \quad \sum f_\alpha \tag{8}$$

$$P \quad \sum g_\alpha \quad \frac{1}{2}u\cdot\nabla\psi(\rho)\delta t \tag{9}$$

$$\rho u c_s^2 \quad \sum e_\alpha g_\alpha \quad \frac{c_s^2}{2}(F_s+G)\delta t \tag{10}$$

And eventually, to calculate the density (ρ) and kinematic viscosity (γ), we have the following:

$$\rho(\phi) \quad \rho_1+\frac{\phi \quad \phi_1}{\phi_2 \quad \phi_1}(\rho_2 \quad \rho_1) \tag{11}$$

$$\gamma(\phi) \quad \gamma_1+\frac{\phi \quad \phi_1}{\phi_2 \quad \phi_1}(\gamma_2 \quad \gamma_1) \tag{12}$$

where γ_1 and γ_2 are the kinematic viscosities, ρ_1 and ρ_2 densities, and ϕ_1 andϕ_2 index functions of the first and second fluid. The values of the index functions are set to 0.2508 and 0.02381 for the heavy and light fluid, respectively.

In non-ideal fluids, $\nabla\psi$ plays a fundamental role in the simulation of intermolecular interactions and separation of phases. This term is obtained from the Carnahan-Starling equation (Ezzatneshan and Vaseghnia, 2020; Ishak et al., 2020; Yuana et al., 2019; Zachariah et al., 2019).

$$\psi(\phi) \quad c_s^2\phi\left[\frac{1+\phi+\phi^2 \quad \phi^3}{(1 \quad \phi)^3} \quad 1\right] \quad a\phi^2 \tag{13}$$

where a represents the power of intermolecular interactions, whose critical value is 3.53357. If a is greater than this value, the flow generated by the movement of the two fluids remains immiscible. It should be noted that, for large values of a, the convergence of the solutions may be disrupted. In the present study, this value is set to 4, and the fourth-order compact scheme has been used for the discretization of $\nabla\psi$.

$$\left(\frac{\partial\psi}{\partial x}\right)_{(i,j)} \quad \frac{1}{3}\left[\psi_{i+1,j} \quad \psi_{i \quad 1,j}\right]+\frac{1}{12}\left[\psi_{i+1,j+1} \quad \psi_{i \quad 1,j \quad 1}\right] + \frac{1}{12}\left[\psi_{i+1,j \quad 1} \quad \psi_{i \quad 1,j+1}\right] \tag{14}$$

$$\left(\frac{\partial\psi}{\partial y}\right)_{(i,j)} \quad \frac{1}{3}\left[\psi_{i,j+1} \quad \psi_{i,j \quad 1}\right]+\frac{1}{12}\left[\psi_{i+1,j+1} \quad \psi_{i \quad 1,j \quad 1}\right] + \frac{1}{12}\left[\psi_{i \quad 1,j+1} \quad \psi_{i+1,j \quad 1}\right] \tag{15}$$

Moreover, the second-order discretization is used For $\nabla^2\psi$ (Lee and Lin, 2005).

$$\nabla^2\psi \quad \frac{1}{6}\left[\psi_{i+1,j+1}+\psi_{i \quad 1,j \quad 1}+\psi_{i \quad 1,j+1}+\psi_{i+1,j \quad 1} +4\left(\psi_{i+1,j}+\psi_{i \quad 1,j}+\psi_{i,j+1}+\psi_{i,j \quad 1}\right) \quad 20\psi_{i,j}\right] \tag{16}$$

Besides, surface tension and gravitational forces are calculated using relations (17) and (18):

$$F_s \quad k\phi\nabla\nabla^2\phi \tag{17}$$

$$G \quad (\rho \quad \rho_m)g \tag{18}$$

In the above equations,ρ_m is defined through the equation$\rho_m \quad (\rho_1+\rho_2)/2$, and k determines a model of surface tension intensity, which is obtained from relations (19) and (20):

$$\sigma \quad k\int\left(\frac{\partial\phi}{\partial\xi}\right)^2 d\xi \quad kI(\alpha) \tag{19}$$

$$I(\alpha) \quad \frac{0.1518(a \quad a_c)^{1.5}}{1+3.385(a \quad a_c)^{0.5}} \tag{20}$$

In Relation (19), ξ is the direction perpendicular to the contact surface.

Considering the type of relations in the He-Chen-Zhang model to obtain the macroscopic characteristics of a fluid, it is not efficient to use the Zou-He boundary condition for obtaining unknown distribution functions at boundaries. Also, the importance of the wall boundary condition in the current problem makes us use the hydrodynamic boundary condition, instead of the bounce-back boundary condition. In what follows, we will detail the way of applying the aforesaid models to obtain unknown distribution functions at boundaries.

2.2. Boundary conditions for the He-Chen-Zhang model

(Noble et al., 1995) introduced the idea of hydrodynamic boundary condition as a different and distinct kind of bounce-back boundary condition. They suggested the use of non-slip conditions to find unknown distribution functions. The easiest and most straightforward way of applying hydrodynamic boundary conditions is using equilibrium conditions at the walls. Special attention should be paid to the fact that after the application of the boundary condition, the streaming process should take place. The streaming distribution functions should not be used to replace the distribution functions at the walls and all the distribution functions should be set to their equilibrium values. Furthermore, the values of the density and velocity of the walls must be used to obtain equilibrium distribution functions at the walls. By developing the boundary condition presented by (Chen et al., 1996), (Guo et al., 2002) introduced a special kind of boundary condition, in which the non-equilibrium part of the distribution functions in the internal points, is extrapolated and added to its equilibrium value at boundaries to obtain the values of distribution functions. It should be noted that this method is of second-order accuracy. Eventually, in the present study, we used a kind of hydrodynamic boundary condition, which is based on the ghost fluid approach and extrapolation of the non-equilibrium values of distribution functions. This kind of boundary condition is of second-order accuracy. In what follows, the way of using this boundary condition is explained in more detail.

Index function (ϕ): By placing the wall among the lattice points and applying the zero gradient to the index functions (with a second-order accuracy), we achieve the following:

$$\phi_{i,0} \quad \phi_{i,1} \ , \ \phi_{i,Ny} \quad \phi_{i,Ny\ 1}\ i \quad 0, Nx \tag{21}$$

where Nx+1 and Ny+1 are the numbers of points in the lattice, in the direction of x and y.

Velocity: Velocities are reflected in mirror forms to apply non-slip and non-penetration conditions.

$$u_{i,0} \quad 2u_w \quad u_{i,1} \ , \ u_{i,Ny} \quad 2u_w \quad u_{i,Ny\ 1}\ i \quad 0, Nx \tag{22}$$

$$v_{i,0} \quad 2v_w \quad v_{i,1} \ , \ v_{i,Ny} \quad 2v_w \quad v_{i,Ny\ 1}\ i \quad 0, Nx \tag{23}$$

In the present study, u_w and v_w are the tangential and vertical velocities of the wall, which are assumed to be zero.

Distribution function (f):

$$f_{i,0} \quad f_{i,0}^{eq} + f_{i,1}^{neq} \ , \ f_{i,Ny} \quad f_{i,Ny0}^{eq} + f_{i,Ny\ 1}^{neq}\ i \quad 0, Nx \tag{24}$$

Pressuredistribution function (g):

$$P_{i,0} \quad P_{i,1} \ , \ P_{i,Ny} \quad P_{i,Ny\ 1}\ i \quad 0, Nx \tag{25}$$

This pressure is used to calculate the equilibrium value of the distribution function (g). But be careful that in order to substitute the velocity in this function, its value must be considered zero, its ghost value must be ignored. By being added to the non-equilibrium value, this equilibrium value creates Function (g) (as in Relation (24) for Function (f)).

In addition to the above-mentioned methods, one of the efficient approaches to obtain unknown distribution functions at boundaries is the extrapolation method for distribution functions at boundaries with known velocities or pressures, which will be discussed in what follows.

In hydrodynamic problems, boundary conditions are usually given for macroscopic values (such as velocitypressure). However, in the lattice Boltzmann method, what is important is knowing the values of distribution functions at boundaries. Hence, there is a need for a comprehensive method to obtain distribution functions based on macroscopic values at the boundaries. Accordingly, researchers proposed the idea of extrapolating the non-equilibrium values of distribution functions similarly to that of hydrodynamic boundary conditions, with the exception that, in the streaming step unlike the hydrodynamic method, distribution functions in internal points can stream into boundariesreplace them (Zhao-Li et al., 2002).

2.3. Simulation of non-Newtonian fluids

Time-independent non-Newtonian fluids are certain kinds of materials, for which the curve of shear stress versus shear rate could not pass through the origin of the coordinate system, or the relationship between may not be linear. The apparent viscosity, which is defined as is a function of The shear rate of these fluids at a certain point of them is determined only by the corresponding shear stress at that point, vice versa. For the generalized Newtonian fluids with no memories of their motion, the uniform shear behavior can be expressed in the form of relation (26):

$$\dot{\gamma}_{yx} \quad f\left(\sigma_{yx}\right) \tag{26}$$

And in its inverse from:

$$\dot{\sigma}_{yx} \quad f^{\ 1}\left(\dot{\gamma}_{yx}\right) \tag{27}$$

According to the above relation, the general behavior of non-Newtonian fluids can be categorized in these three types:

1 Shear-thinning or pseudoplastic behavior
2 Viscoplastic behavior
3 Shear-thickening or dilatant behavior

However, for time-dependent fluids the apparent viscosity changes with timeshear rate (Abedi et al., 2020). In other words, they can be termed as memory materials. Examples of these types of fluids are gelatine, shortening, cream, paints, yogurt, xanthan gum solutions, aqueous iron oxide gels, gelatine gels, pectin gels, synovial fluid, hydrogenated castor oil, some clays (including bentonite, montmorillonite), carbon black suspension in molten tire rubber, some drilling muds, many paints, many floc suspensions, many colloidal suspensions. According to the time-dependent viscosity model (Larson, 2015), the apparent viscosity of the fluid is obtained from Relation (28).

$$\mu \quad \mu_{21} + (\mu_{22} \quad \mu_{21})\ S \tag{28}$$

where

$$\frac{DS}{Dt} \quad a(1 \quad S) \quad b S\dot{\gamma} \tag{29}$$

In Relations (28) (29), (a,b) are the viscosity curve fitting constantsstructural parameter (s) is an index of the degree of microstructures within the fluid system which lies in the range of 0–1. The fluid's viscosities corresponding to these two limiting cases are denoted by $\mu_{21}\mu_{22}$, respectively. Finally, the value of the shear rate tensor is obtained from relations (30) (31).

$$\dot{\gamma} \quad \nabla V + \nabla V^T \tag{30}$$

$$|\dot{\gamma}| \quad \sqrt{\frac{1}{2}\dot{\gamma} : \dot{\gamma}} \tag{31}$$

In the lattice Boltzmann method, the relaxation time is considered to be constant for Newtonian fluids at any point of the lattice. But, for non-Newtonian fluids, the relaxation time at each point is different from that at its adjacent point. It should be noted that in time-dependent fluids, the viscosity is a function of time, velocity gradient, shear history. Thus, because of differences in the velocity gradient, viscosityrelaxation time at each point are different from those at its neighborhood.

2.4. Simulation of the temperature field

The distribution function (T) is utilized by the thermal lattice

Boltzmann model for the temperature field (Mohamad, 2011). The general form of the Lattice Boltzmann equation For the temperature field is as follows:

$$T_\alpha(x+e_\alpha\delta t, t+\delta t) \quad T_\alpha(x,t) \qquad \frac{T_\alpha(x,t) \quad T_\alpha^{eq}(x,t)}{\tau_T} \tag{32}$$

where the equilibrium distribution functionrelaxation time for the temperature field defined as:

$$T_\alpha^{eq}(u) \quad t_\alpha temp\left[1+\frac{e_\alpha \cdot u}{c_s^2}\right] \tag{33}$$

$$\tau_T \quad 3\alpha + 0.5 \tag{34}$$

In the above equations, α is the thermal diffusion coefficienttemp is local temperature. Finally, the distribution functions (f, g) which introduced in the previous sectionT are coupled through the following force term:

$$F_b \quad \rho g\beta\left(temp \quad temp_{ref}\right) \tag{35}$$

where β is the thermal expansion coefficient$temp_{ref}$ is the reference temperature (cold wall or ambient temperature) usually set to 0 in the non-dimensional scale. The buoyancy force couples the Navier–Stokes equation with energy equation. It is assumed that invading fluid enters the channel with a specific temperature. Also, bottomtop of the channel are maintained at fixed temperatures.

2.5. Lattice Boltzmann model for nanofluid

Because of differences in thermo-physical properties such as density, thermal conductivity, specific heat capacitythermal expansion, both hydrodynamicthermal properties of nanofluid are different from those of pure fluid. Hence, the governing equations of the mixture must be modified precisely. Therefore, the density, thermal expansion, heat capacity, thermal diffusion, dynamic viscositythermal conductivity are given by the following relations, respectively.

$$\rho_{nf} \quad (1 \quad \phi)\,\rho_f + \phi\,\rho_s \tag{36}$$

$$\beta_{nf} \quad (1 \quad \phi)\,\beta_f + \phi\,\beta_s \tag{37}$$

$$\left(\rho c_p\right)_{nf} \quad (1 \quad \phi)\,\left(\rho c_p\right)_f + \phi\,\left(\rho c_p\right)_s \tag{38}$$

$$\alpha_{nf} \quad \frac{\alpha_{nf}}{\left(\rho c_p\right)_{nf}} \tag{39}$$

$$\mu_{nf} \quad \frac{\mu_f}{1 \quad \phi^{2.5}} \tag{40}$$

$$k_{nf} \quad k_f\left[\frac{k_s + 2k_f + 2\phi\left(k_s \quad k_f\right)}{k_s + 2k_f \quad \phi\left(k_s \quad k_f\right)}\right] \tag{41}$$

In the above relations f, snf represent pure fluid, nanoparticlesmixture properties.

2.6. Simulation of the electric field

In the present study, the leaky dielectric model is used to simulate the effects of applied electric fields on displacement flow. In our simulations, the electric field is considered to be irrotational. It means:

$$\nabla \times \vec{E} \quad 0 \tag{42}$$

where E is the electric field. The electric force applied to a fluid element can be written as:

$$\vec{F} \quad \int\left(\rho\vec{E} \quad \frac{1}{2}E^2\nabla\varepsilon\right)dx^3 \tag{43}$$

In the above equation, ε is the local fluid permittivity. The forces experienced by fluid particles can be expressed as a Maxwell stress tensor or as a body force. Therefore, the influence of an applied electric field on the fluid motion is created by this electric force (Almasi et al., 2019):

$$\vec{F} \qquad \frac{1}{2}\vec{E}\cdot\vec{E}\nabla\varepsilon + q\vec{E} \tag{44}$$

where q is the free charge density given by:

$$q \quad \nabla\cdot\left(\varepsilon\vec{E}\right) \tag{45}$$

The electric field can be written as the gradient of a scalar potential U.

$$\vec{E} \qquad \nabla U \tag{46}$$

Also, the mixture dielectric properties (local fluid permittivity-conductivity) are assumed as follows:

$$\varepsilon(\phi) \quad \varepsilon_1 + \frac{\phi \quad \phi_1}{\phi_2 \quad \phi_1}(\varepsilon_2 \quad \varepsilon_1) \tag{47}$$

$$\chi(\phi) \quad \chi_1 + \frac{\phi \quad \phi_1}{\phi_2 \quad \phi_1}(\chi_2 \quad \chi_1) \tag{48}$$

where ε_1, ε_2, $\chi_1\chi_2$ are constants which can be adjusted to produce different bulk property values.

In this study, the lattice Boltzmann framework proposed by HeLi (2000) is followed to solve the electric potential. Thus, a new set of particle distributions is introducedtheir evolutions are described as:

$$h_\alpha(x+e_\alpha\delta t, t+\delta t) \quad h_\alpha(x,t) \qquad \frac{h_\alpha(x,t) \quad h_\alpha^{eq}(x,t)}{\tau_h} \tag{49}$$

where equilibrium distribution functionrelaxation time for electric field are:

$$h_\alpha^{eq} \quad t_\alpha U \tag{50}$$

$$\tau_h \quad 3\sigma + 0.5 \tag{51}$$

Finally, potential U is defined as:

$$U \quad \sum_\alpha h_\alpha \tag{52}$$

The potential U at northernsouthern boundaries is known. Also, the open boundary condition is set at the inletoutlet. Therefore, like temperature distribution functions we have:

2.7. Simulation of magnetic force

In this study uniform magnetic field ($\vec{B} \quad B_x\vec{e}_x + B_y\vec{e}_y$) is applied to the domain of solution. The orientation of the magnetic field forms an angle γ with the horizontal axis of the channel such that γ

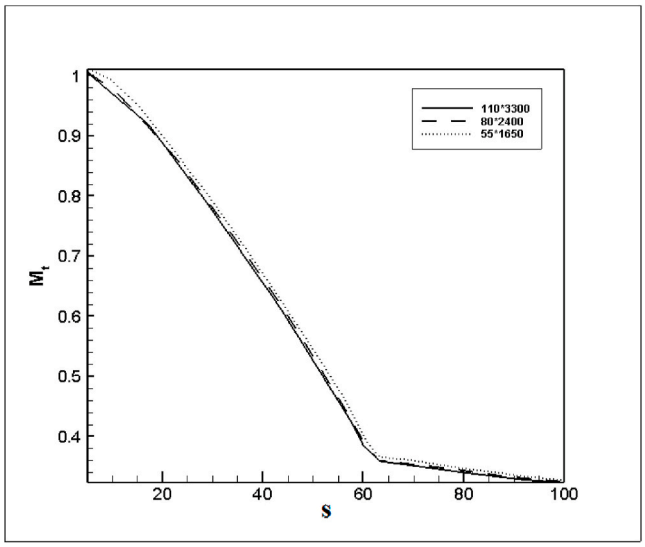

Fig. 2. The effects of changes in the lattice layout on changes in M_t at different times.

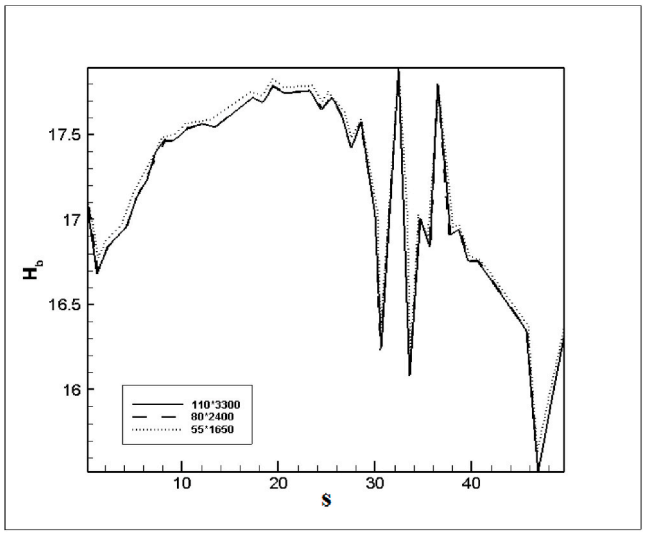

Fig. 3. The effects of changes in the lattice layout on the mean thickness of the static layer left on the lower wall of the channel at different times.

$\cot^{-1}(B_x/B_y)$. The electromagnetic force F is defined by $\vec{F}$ $\xi(\vec{V} \times \vec{B}) \times \vec{B}$. In order to incorporate this force term in the model, it needs to be calculated in the two directions as follows (Kefayati et al., 2012):

$$F_x \quad \frac{Ha^2\mu_{nf}}{H^2}\left(v\sin\gamma\cos\gamma \quad u\sin^2\gamma\right) \tag{53}$$

$$F_y \quad \frac{Ha^2\mu_{nf}}{H^2}\left(u\sin\gamma\cos\gamma \quad v\cos^2\gamma\right) \tag{54}$$

where H is the height of the channelthe Hartmann number is defined as:

$$Ha \quad HB_0\sqrt{\frac{\sigma_{nf}}{\mu_{nf}}} \tag{55}$$

2.8. Modeling procedure

In the numerical solution, the new relaxation time at each point (τ) is related to the velocity gradienttime. This new value will be used it in the next time step. So, the general procedure of the numerical solution will be as follows:

1) Initialization of distribution functionsrelaxation time
2) Calculation of the macroscopic velocity fielddensity
3) Calculation of equilibrium distribution functions
4) Calculation of the velocity gradient
5) Calculation of viscosity using the structural equation of non-Newtonian fluids
6) Calculation of the new relaxation time for non-Newtonian fluids
7) Calculation of new distribution functions in the collision step
8) Stream distribution functions into their adjacent points (propagation step)
9) Using new relaxation time, velocity field, distribution functions in the next time step (Step 2)repetition of this process

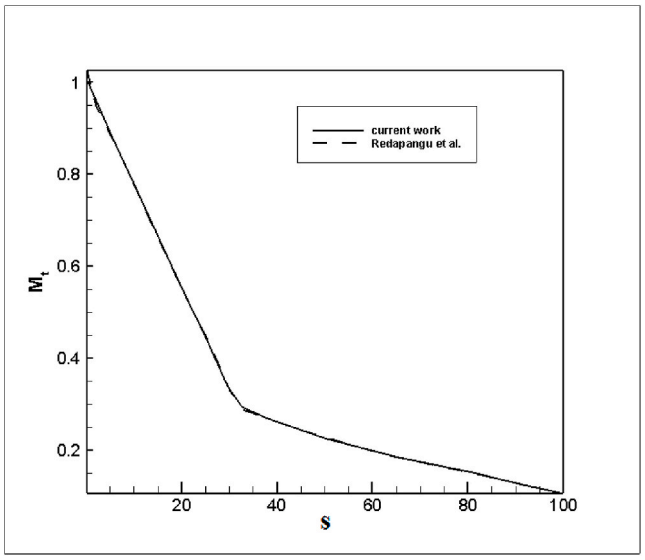

Fig. 4. A comparison between the results of the present studythe results obtained by Redapangu et al. [11] for At = 0, m = 2, Ri = 0, Ca = 0.263, Re = 100,L/H = 48 in a horizontal channel.

3. Lattice independence ofvalidation of the computer code

In order to explain the factors affecting the characteristics of a flow, we have used the following non-dimensional numbers: Reynolds (Re $Q\rho_1/\mu_1$), Atwood (At $(\rho_2 \quad \rho_1)/(\rho_2 + \rho_1)$), viscosity ratio ($m$ μ_2/μ_1), Richardson (Ri gH^3/Q^2), Rayleigh (Ra $g\beta\Delta tempH^3/\nu_1\alpha_1$), Prandtl ($Pr$ ν_1/α_1)capillary (Ca $Q\mu_1/\sigma H$). In the above-mentioned relations, Q is the volumetric flow rate per unit length.

Fig. 2 shows time changes in the dimensionless volume (M_t M_x/M_0) of Fluid 2 for At 0.2, m 2, Ri 0.1, Ca ∞, Re 100,θ 45 in the three lattice layouts; 55 × 1650, 80 × 2400,110 × 3300, where; S is the dimensionless time,M_0M_x are criteria for the initial volumetime-varying volume of Fluid 2, which are calculated through relations (81) to (83):

$$S \quad H^2/Q \tag{56}$$

$$M_0 \quad \frac{\phi \quad \phi_1}{\phi_2 \quad \phi_1}LH \tag{57}$$

$$M_x \quad \int_0^L\int_0^H \frac{\phi \quad \phi_1}{\phi_2 \quad \phi_1}dydx \tag{58}$$

And Fig. 3 shows changes in the mean thickness of the static layer left on the lower wall of the channel for At 0.2, m 20, Ri 1, Ca ∞, Re

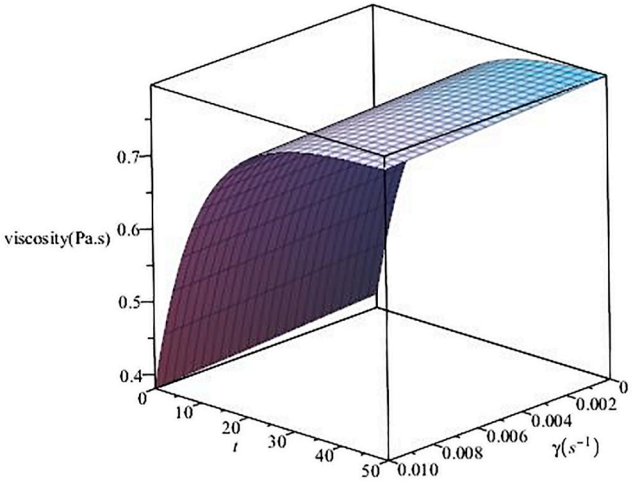

Fig. 5. Viscosity changes versus timeshear rates in time-dependent fluids for a = 0.1, b = 0.5.μ_{21} = 0.4μ_{22} = 0.8

100,θ 45 using definitions (84) (85) for the lowerupper walls, respectively:

$$H_b \quad \frac{1}{x_l \quad x_b} \int_{x_b}^{x_l} \int_{0}^{Ny/2} \frac{\phi \quad \phi_1}{\phi_2 \quad \phi_1} dydx \tag{59}$$

$$H_t \quad \frac{1}{x_l \quad x_t} \int_{x_t}^{x_l} \int_{Ny/2}^{Ny} \frac{\phi \quad \phi_1}{\phi_2 \quad \phi_1} dydx \tag{60}$$

Eventually, due to the low difference between the results of the two denser layouts, the appropriate structure has been taken into consideration. We also used the results obtained by Redapangu et al. [11] for a simple Newtonian displacement in a horizontal channel with At 0, m 2, Ri 0, Ca 0.263,Re 100 (as shown in Fig. 4) to verify the performed simulation.

4. ResultsDiscussion

In the current study, traditional approaches of the Lattice Boltzmann method were utilized to simulate the temperatureelectric field. Application of these fields results in creating new external forces which can be added to the interfacial forces in step 2. Before analyzing the presented results, the type of viscosity changes versus timeshear rates is shown in Fig. 5 (for a 0.1, b 0.5, μ_{21} 0.4μ_{22} 0.8).

It can be seen that for a specific shear rate, the viscosity increases with the time. In addition, at a fixed time point, a higher shear rate leads to enhancement of viscosity. The occurrence of such behavior in the trend of viscosity changes versus timeshear rates plays a key role in interpreting the dynamicsefficiency of the displacements.

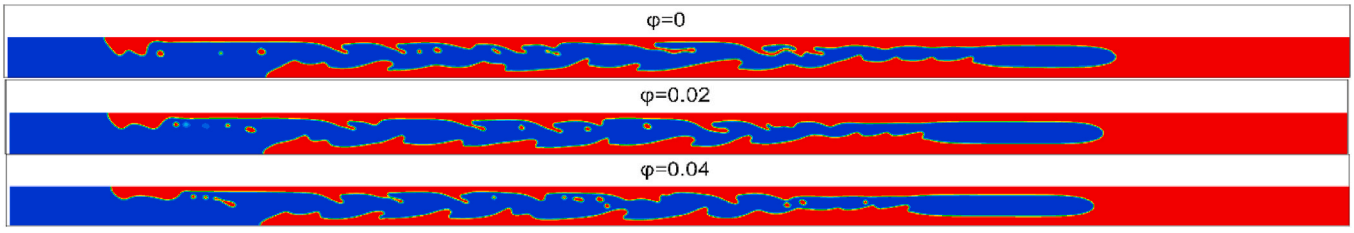

Fig. 6. The effect of nanoparticles on the density contour in displacements of time-dependent fluids for the parameters listed in Table 1.

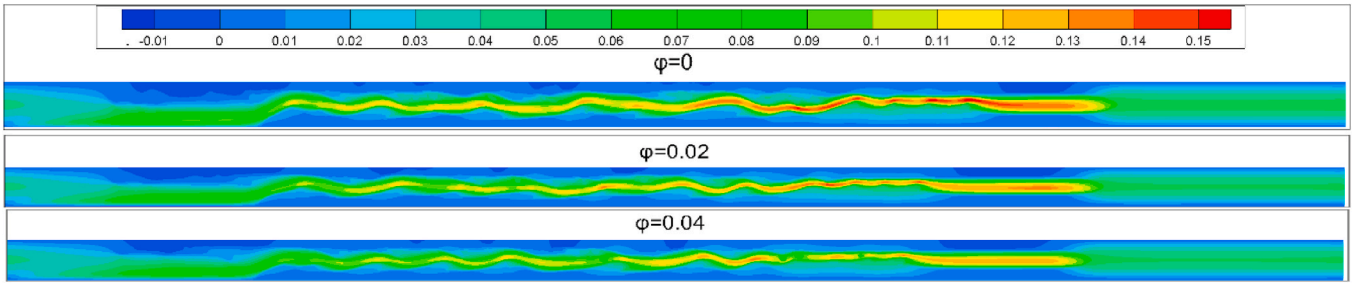

Fig. 7. The effect of nanoparticles on the longitudinal velocity contour in displacements of time-dependent fluids for the parameters listed in Table 1.

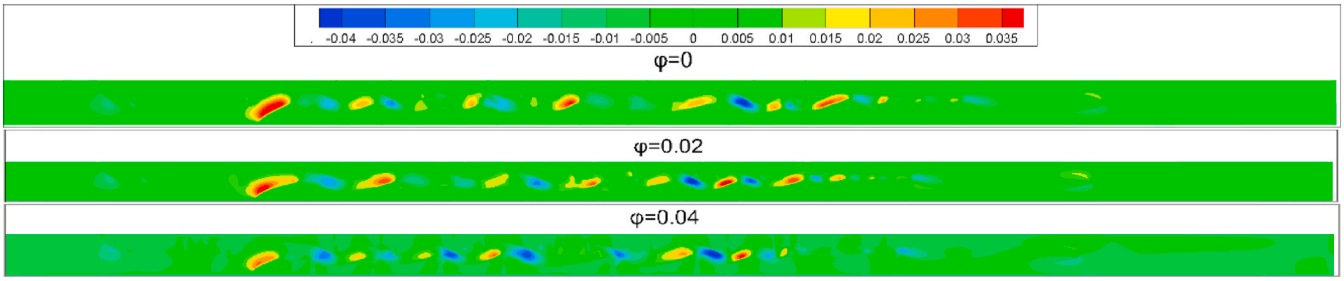

Fig. 8. The effect of nanoparticles on the transverse velocity contour in displacements of time-dependent fluids for the parameters listed in Table 1.

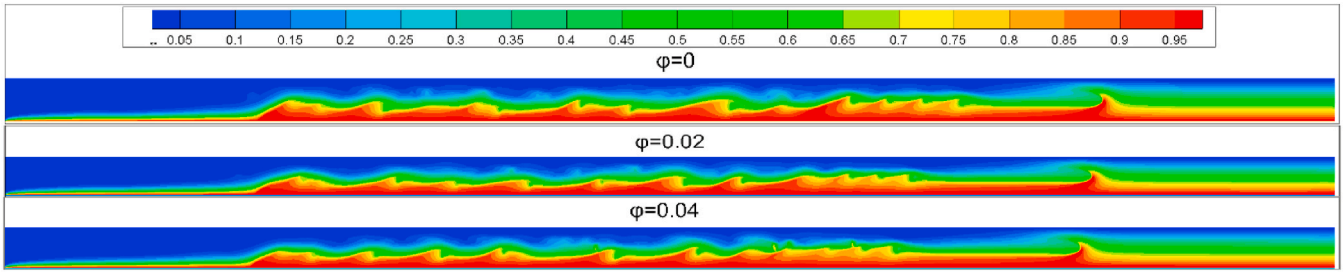

Fig. 9. The effect of nanoparticles on the temperature contour in displacements of time-dependent fluids for the parameters listed in Table 1.

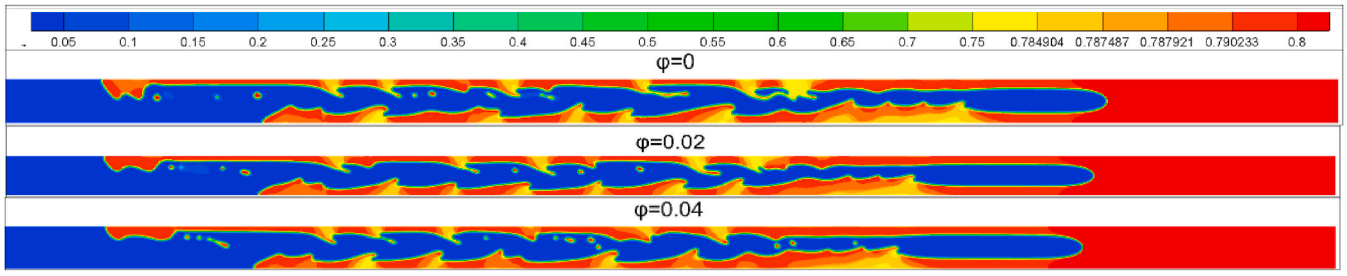

Fig. 10. The effect of nanoparticles on the viscosity contour in displacements of time-dependent fluids for the parameters listed in Table 1.

Table 1
Dimensionless numbersparameters used in simulation.

m	Re	Ri	At	Ca	Angle of Inclination	Pr	Ra	α_1/α_2	a	b	μ_{21}	μ_{22}	T
20	100	1	0.2	0.25	45	1	20,000	0.2	0.1	0.5	0.4	0.8	50

Table 2
Thermo-physical properties of pure injected fluidnanoparticles.

	ρ(Kg /m^3)	β(K ^{1})	C_P(J/kg K)	k(w/m K)
Pure fluid	1000	0.0002	4000	0.5
nanoparticle	4000	0.00016	600	10

4.1. *Effects of added nanoparticles*

By defining t 1000δt Figs. 6–10 show the effects of nanoparticles on the flow dynamics in pressure-driven displacements of time-dependent fluids for the parameters listed in table. 1and ϕ 0, ϕ 0.02, ϕ 0.04. These figures qualitatively reveal the effect of nanoparticles on the contours of density, longitudinal velocity, transverse velocity, temperatureviscosity.

Adding nanoparticles to displacing fluid changes the displacement efficiency through various mechanisms. The increment in the density-decrement in the thermal expansion coefficient of injected fluid (caused

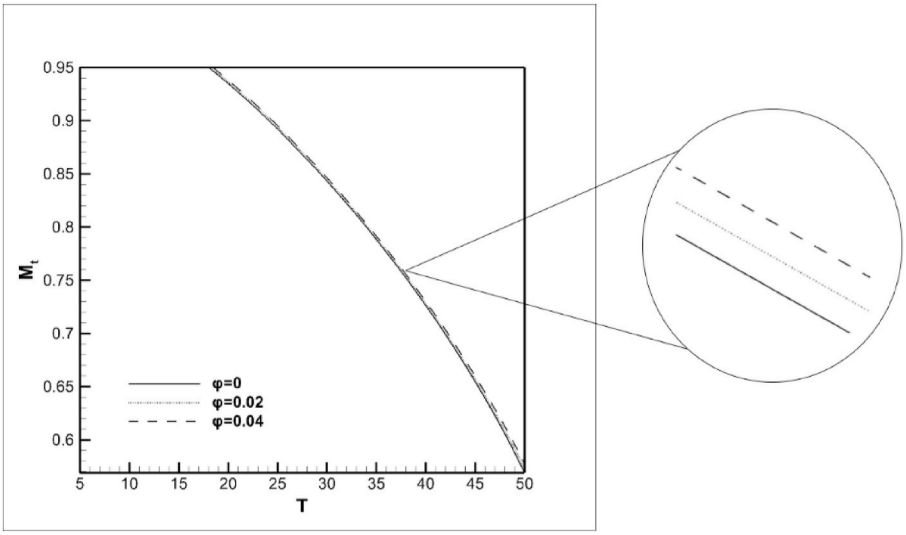

Fig. 11. Displacement efficiency versus time for time-dependent fluidsdifferent (ϕ)s.

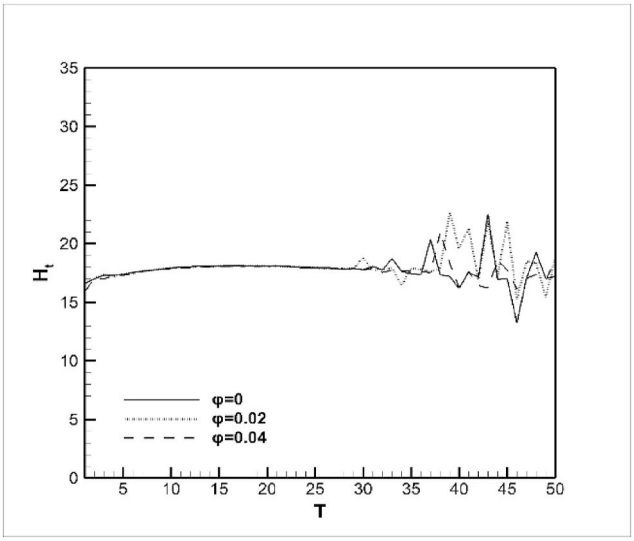

Fig. 12. The mean thickness of the static layer versus time at the top of the channel in the displacement of time-dependent fluids for different (ϕ)s.

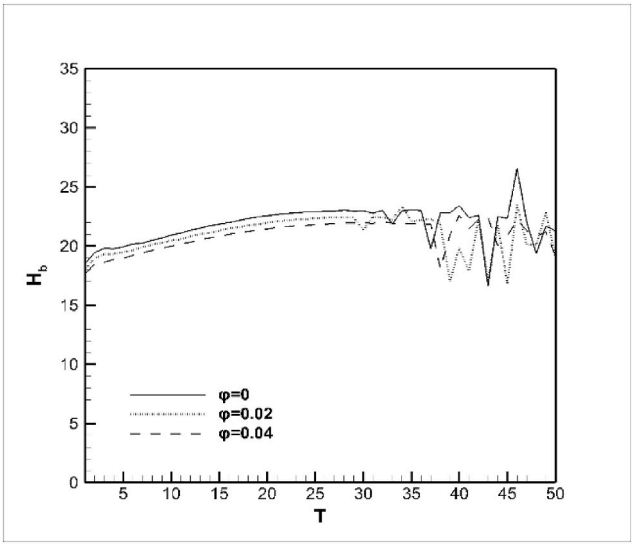

Fig. 13. The mean thickness of the static layer versus time at the bottom of the channel in the displacement of time-dependent fluids for different (ϕ)s.

by adding nanoparticles) enhances the vertical forcesthat in turn increases the vertical motion of this fluid toward the bottom of the channel. On the other hand, a higher viscosity of invading mixture causes the momentum transfer between its layers to occur more severely. Finally, alteration in the specific heat transferconduction leads to change in relaxation time, the equilibrium distribution function of temperature, total temperaturevertical motion of displacing fluid. The thermo-physical properties of pure injected fluidnanoparticles are presented in Table 2.

Figs. 11–13 exhibit the total efficiency of displacementthe thickness of the static layers at the topbottom of the channel respectively. According to the above-mentioned explanation, increasing in densityviscosity of injected fluid improves its ability for driving the secondary one. However, the effects of this improvement on the displacement efficiency are very small (Fig. 11). On the other hand, the influences of variation in the thermal features of injected fluid are not enough to change the thickness of the static layers significantly. It should be mentioned that because of the economical considerations percent of nanoparticles cannot be enhanced greatly. So, adding nanoparticles to the injected fluid is not an appropriate way to change the displacement efficiency.

4.2. *Effects of applying electric field*

By defining E_0 $(U_{upper}$ $U_{lower})/H$, Figs. 14–20 show the effects of electro-hydrodynamics on the flow dynamics in pressure-driven displacements of time-dependent fluids for the parameters listed in Table 1E_0 0, E_0 0.05, E_0 0.1.

The effects of electric field on transverse forces at the interface of two fluids cause wide changes in the appearance of the displacement. According to Fig. 19, these transverse forces at the upper interface are toward the top of the channel. However, they are toward the bottom of the channel at the lower interface. The sign change of these forces has roots in the variation of $\nabla\varepsilon$ value (Relation. 57) at different points of the interface. In the present study, X_t is used to represent the front of the invading fluid flow at the top of the channelX_b for that at the bottom of the channel. Moreover, as an important criterion for determining the advance of the displacing fluid, we identified the point of the displacing fluid, which has the maximum value in the direction of the x-axis. This location is represented by $X_L$called the attacking front Fig. 21. As shown in Figs. 22–25, increasing lateral forces at the interface points toward the walls of the channel causes an increment in the location of X_tX_b. Although, decrement in the location of X_L is associated with the reduction in axial motion of the invading fluid. As a result, the total efficiency of displacement (M_t) doesn't change significantly. Based on definitions (86) (87), Fig. 26Fig. 27 show the flow efficiency in all the longitudinalcross sections of the channel, the advance rate of the displacing fluidthe severity of interfacial instabilities.

$$R_x \quad \frac{1}{H}\int_0^H \frac{\phi \quad \phi_1}{\phi_2 \quad \phi_1}\,dy \tag{61}$$

$$R_y \quad \frac{1}{L}\int_0^L \frac{\phi \quad \phi_1}{\phi_2 \quad \phi_1}\,dx \tag{62}$$

Regarding previous explanations, the enhancement in the power of the electric fieldmotion of the injected fluid toward the walls of the channel can be interpreted as an improvement in displacement efficiency in longitudinal sections close to the wallsvice versa. It should be mentioned that imposing higher electric field intensifies interfacial instabilities which appear as fluctuations in R_x (Fig. 26)discontinuous finger structure in density contour (Fig. 14). Thus, a strong electric field

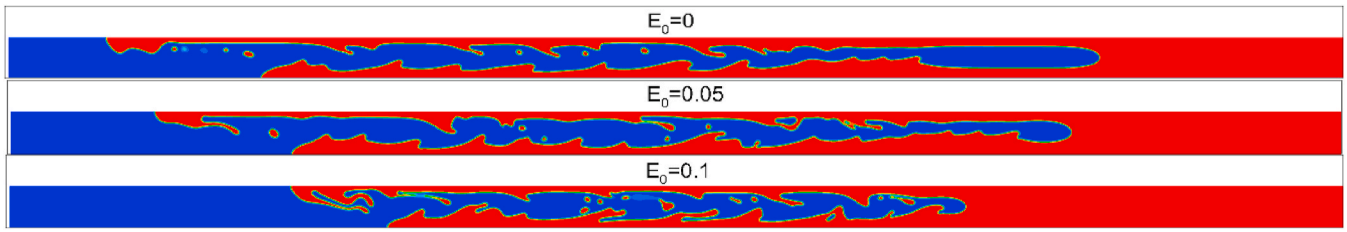

Fig. 14. The electro-hydrodynamics effects on the density contour in pressure-driven displacements of time-dependent fluids for the parameters listed in Table 1.

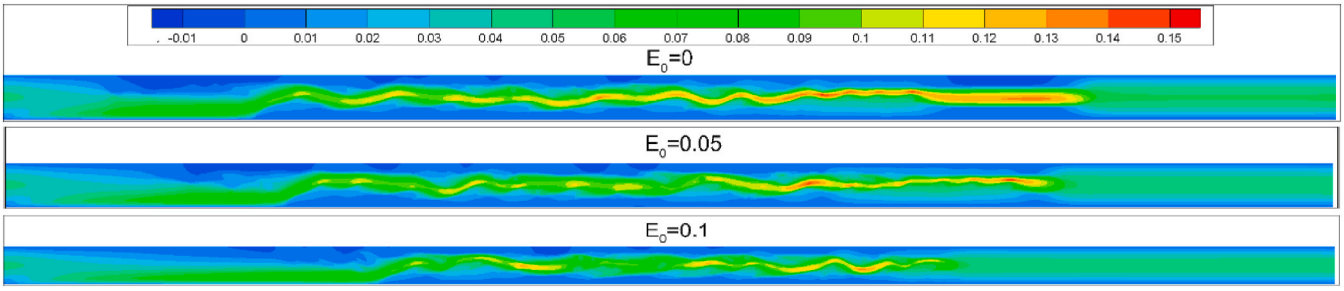

Fig. 15. The electro-hydrodynamics effects on the longitudinal velocity contour in pressure-driven displacements of time-dependent fluids for the parameters listed in Table 1.

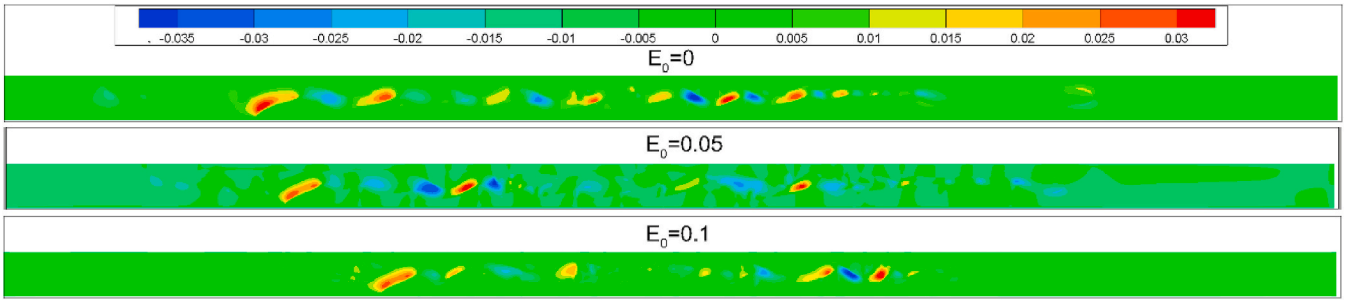

Fig. 16. The electro-hydrodynamics effects on the transverse velocity contour in pressure-driven displacements of time-dependent fluids for the parameters listed in Table 1.

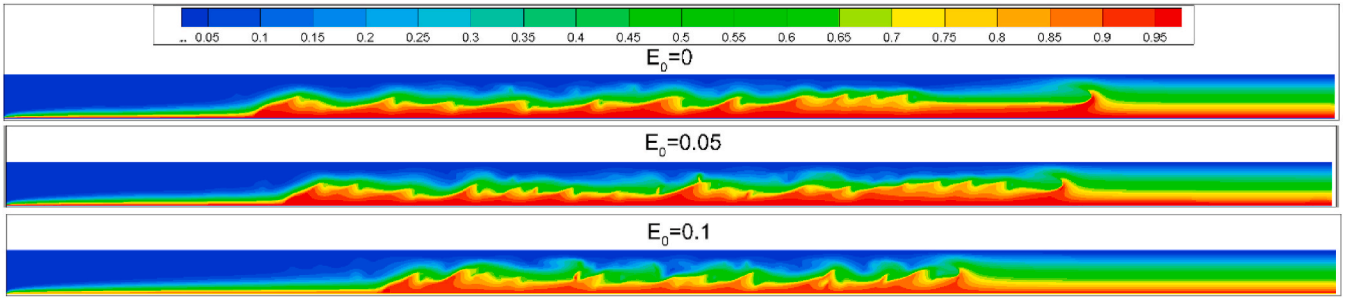

Fig. 17. The electro-hydrodynamics effects on the temperature contour in pressure-driven displacements of time-dependent fluids for the parameters listed in Table 1.

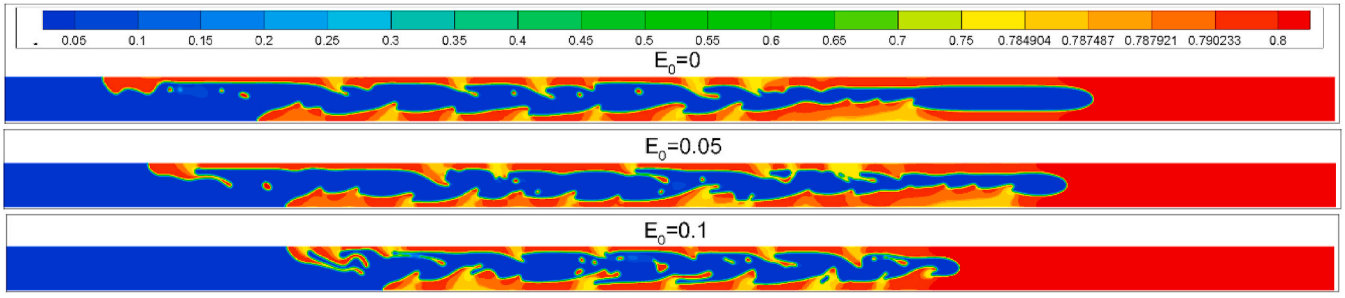

Fig. 18. The electro-hydrodynamics effects on the viscosity contour in pressure-driven displacements of time-dependent fluids for the parameters listed in Table 1.

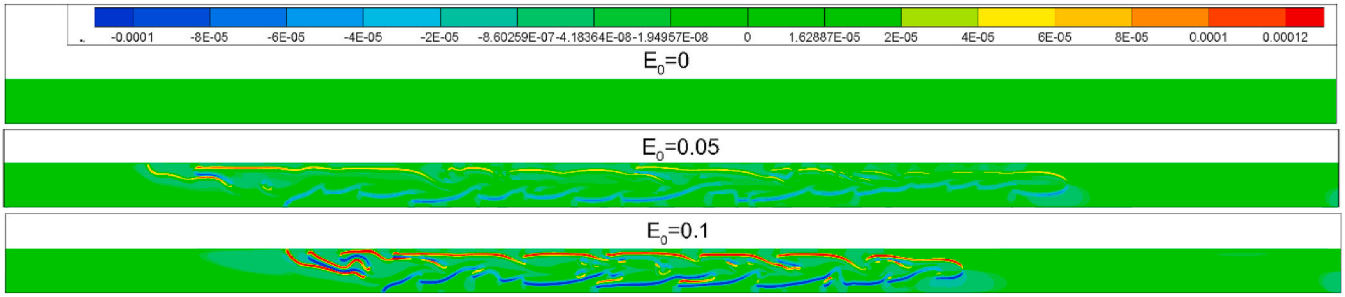

Fig. 19. The electro-hydrodynamics effects on the transverse force contour in pressure-driven displacements of time-dependent fluids for the parameters listed in Table 1.

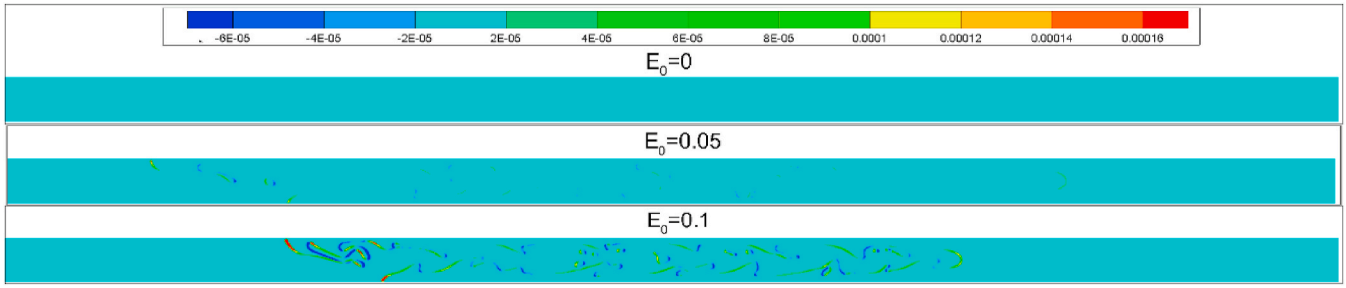

Fig. 20. The electro-hydrodynamics effects on the longitudinal force contour in pressure-driven displacements of time-dependent fluids for the parameters listed in Table 1.

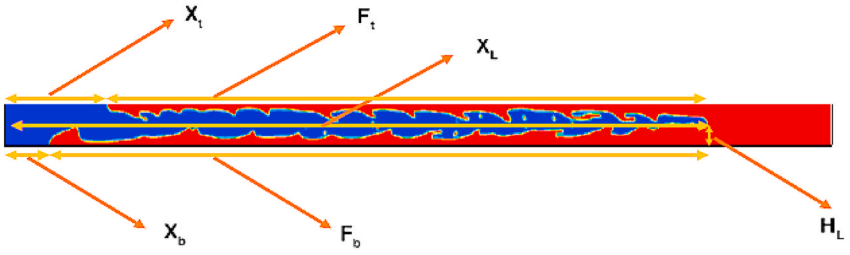

Fig. 21. A schematic showing the appearance of the displacement.

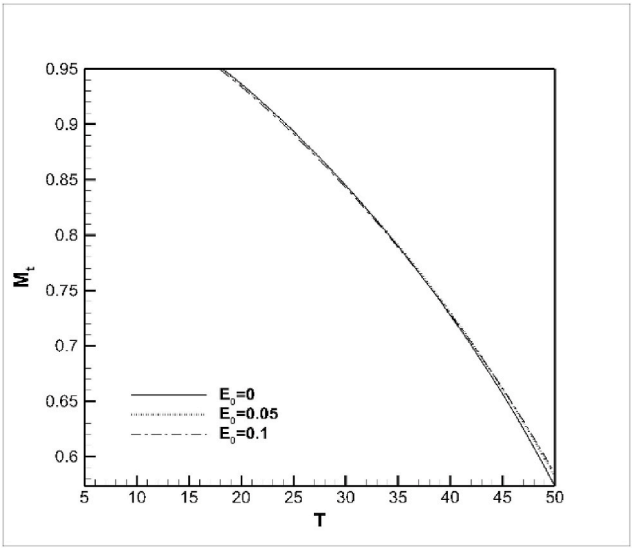

Fig. 22. Displacement efficiency versus time for different (E_0)s in the displacement of time-dependent fluids.

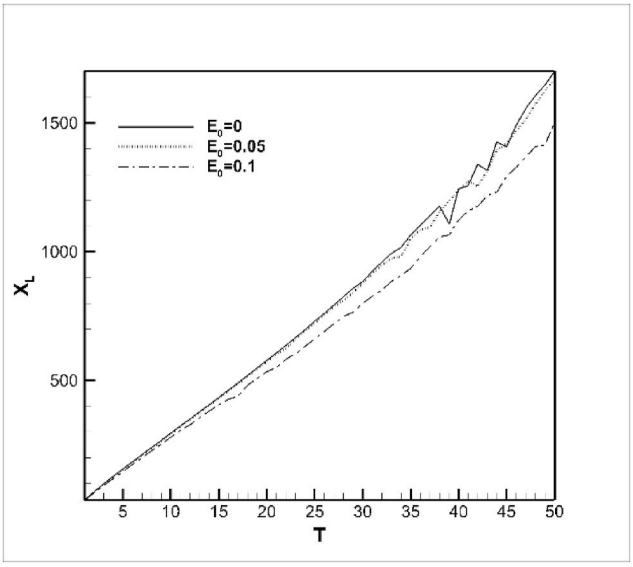

Fig. 23. The location of the attacking front versus time for different (E_0)s in the displacement of time-dependent fluids.

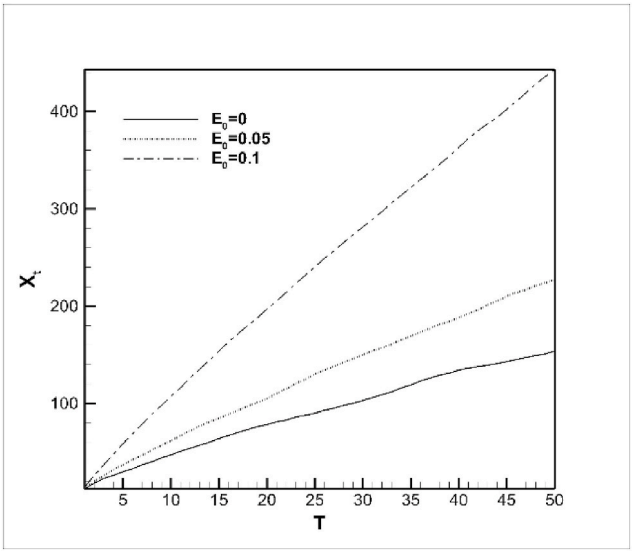

Fig. 24. The location of the advancing front at the top of the channel versus time for different (E_0)s in the displacement of time-dependent fluids.

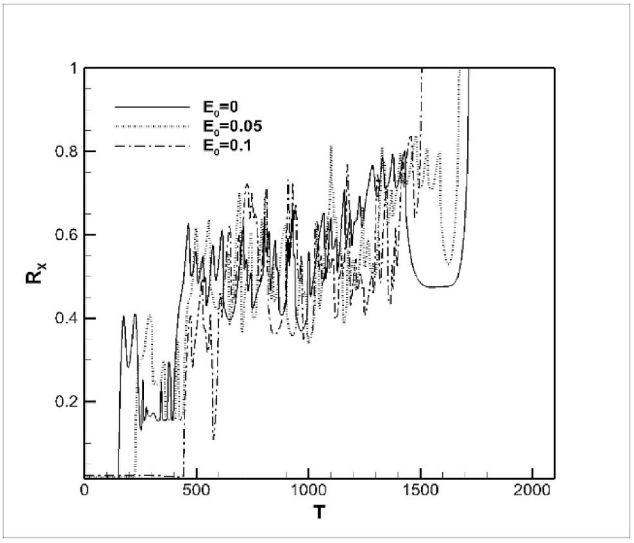

Fig. 26. The efficiency versus R_x for different (E_0)s in the displacement of time-dependent fluids.

increases the average thickness of the static layers at the topbottom of

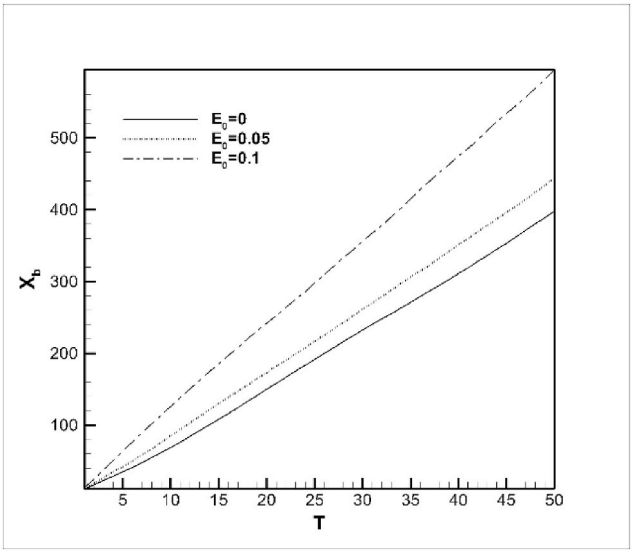

Fig. 25. The location of the advancing front at the bottom of the channel versus time for different (E_0)s in the displacement of time-dependent fluids.

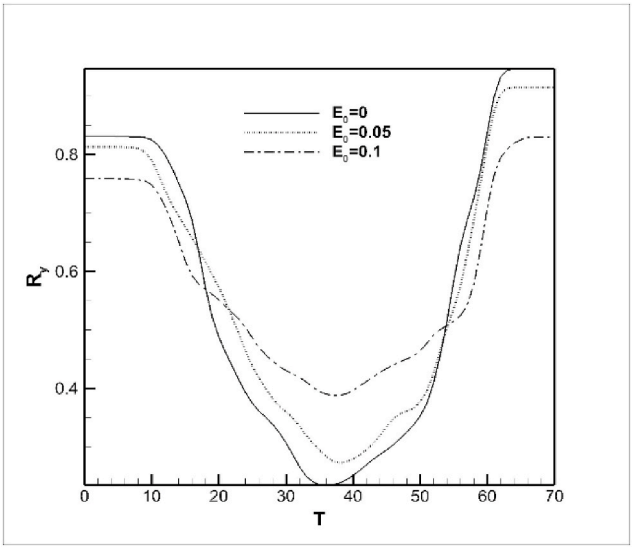

Fig. 27. The efficiency versus R_y for different (E_0)s in the displacement of time-dependent fluids.

the channel (Fig. 2829). Enhancing interfacial forces magnifies velocity in the same direction. As a result, by intensifying small perturbations at the interface of two fluids, the magnitude of interfacial instabilities increases. Nevertheless, altering roll-up structure, vorticities, temperature distribution control Kelvin-Helmholtz, Reighley-Taylor,Reighley-Benard instabilities. Finally, the equal total efficiency (M_t) for different values of E_0 implies that the area under the curves R_xR_y is equal for all of the cases.

It is worth mentioning that the static wall layer left on the lower wall is exposed to the warmer boundary for a long time. So, this region has a higher temperature in comparison with other areas of the flow. This layer at the top of the channel has a lower temperature, Because not only it is located in the neighborhood of the colder boundary, but also a continuous flow of the cold finger-like structure prevents the upper layer from sticking to lower one. Eventually, according to Fig. 5 the viscosity of the time-dependent fluid reaches its maximum value after a long timesmall deviation from this value in Fig. 18 is related to the differences in the velocity gradient in various points of the channel.

4.3. *Effects of applying magnetic field*

Figs. 30–35 show the effects of magneto-hydrodynamics on the flow dynamics in pressure-driven displacements of time-dependent fluids for the parameters listed in Table 1, θ 0, θ 180Ha 0, Ha 10.

In order to intensify magnetic forces in the direction (or opposite direction) of transverse velocity the coordinate system is turned as Fig. 36 (just for calculating ((V × B) × B)).

In the simulation of the magnetic forces, the electrical conductivity of the displaced fluid is assumed to be ignorable in comparison to those

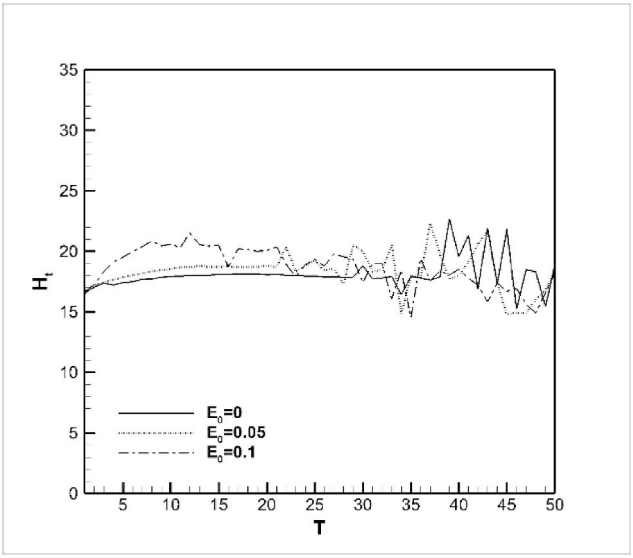

Fig. 28. The mean thickness of the static layer versus time at the top of the channel in the displacement of time-dependent fluids for different (E_0)s.

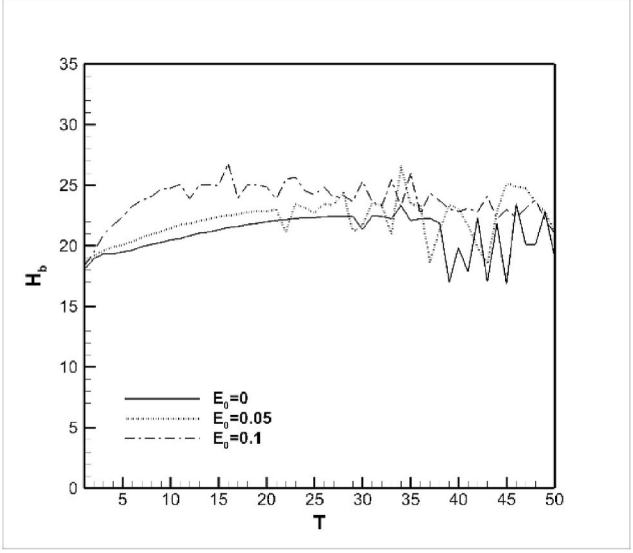

Fig. 29. The mean thickness of the static layer versus time at the bottom of the channel in the displacement of time-dependent fluids for different (E_0)s.

of the injected fluid. Therefore, these forces just impress the displacing fluid. According to Figs. 30–32 for Ha 10θ 180 resisting forces against the transverse movement of the displacing fluid regularize the finger structure. Thus, the axial motion of this fluid occurs in a wider space. So, injection of cold invading fluid to warm static layer reduces.

According to the above explanations, for Ha 10θ 180, by enhancing axial velocity of the invading fluid, its ability of displacing increases. On the other hand, for Ha 10θ 0, the magnetic forces intensify transverse motion of the injected fluid toward the walls. So, $M_t$the locations of X_L , X_tX_b are representatives of these behaviors (Figs. 37–40).

Three effective factors which determine the average thickness of the static wall layers are displacement efficiency in the different cross-sections of the channel, development of interfacial instabilitiesdisplacing fluid tendency to move toward the walls. For Ha 10θ 0, enhancement of this tendency in longitudinal sections close to the channel walls causes the displacement efficiency to increase. However, this motion (toward the walls) is associated with a decrement in the displacement efficiency for longitudinal sections close to the channel axis (Fig. 42). In contrast to the effects of the electric field, imposing a magnetic field creates a special kind of transverse motion in the displacing fluid which finally leads to enhancement in the total efficiency of displacement. It means in comparison with induced interfacial force by the electric field, the body force generated by applying the magnetic field doesn't violate the integrity of the fingering structure. The average thickness of the static wall layer is calculated for y 0 to y $N_y/2$y $N_y/2$ to y N_y (Relation. 8485). Finally, for Ha 10θ 0, with the transverse velocity increasing, interfacial instabilities (Fig. 41) which are the main cause of the fluctuations in the average thickness of the static wall layers, enhance (Fig. 4344).

5. Conclusion

In this study, the He-Chen-Zhang model is used to simulate the displacement of a time-dependent non-Newtonian fluid by a Newtonian one. We have numerically investigated the effects of heating channel wallsapplying magnetic/electric fields on added nanoparticles to improve the efficiency this transport process. Several diagramsfigures are provided to demonstrate the displacement efficiencythe apparent flow pattern at different cross-sections of the channel.

The results of our simulations revealed that imposing higher electric field intensifies interfacial instabilities due to increment in the transverse velocity. However, the total efficiency of the displacement (M_t) does not change significantly. It means applying the electric field is the best approach to sweep the residual boundary layer of the displaced fluid around the fingering structure. But, we cannot expect to collect higher amount of secondary fluid for injecting a specific volume of Newtonian fluid over time.

By increasing the Hartmann numberchanging the rotation angle of the coordinate system (to 180), the resisting forces against transverse movement of the displacing fluid are intensified. Hence, axial velocity of

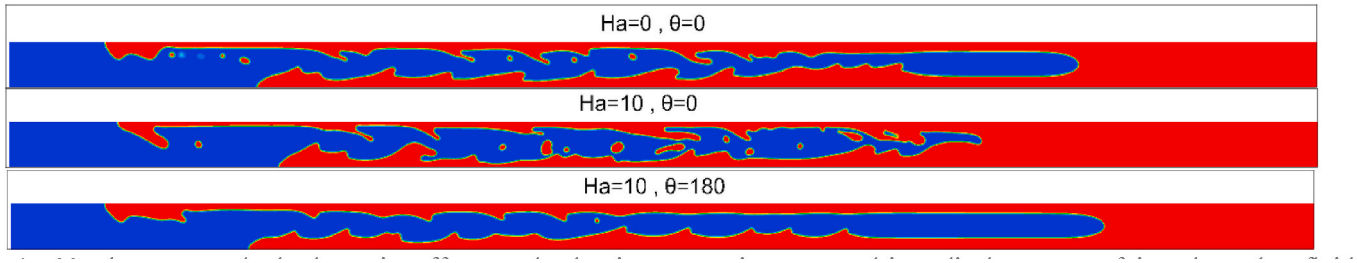

Fig. 30. The magneto-hydrodynamics effects on the density contour in pressure-driven displacements of time-dependent fluids for the parameters listed in Table 1.

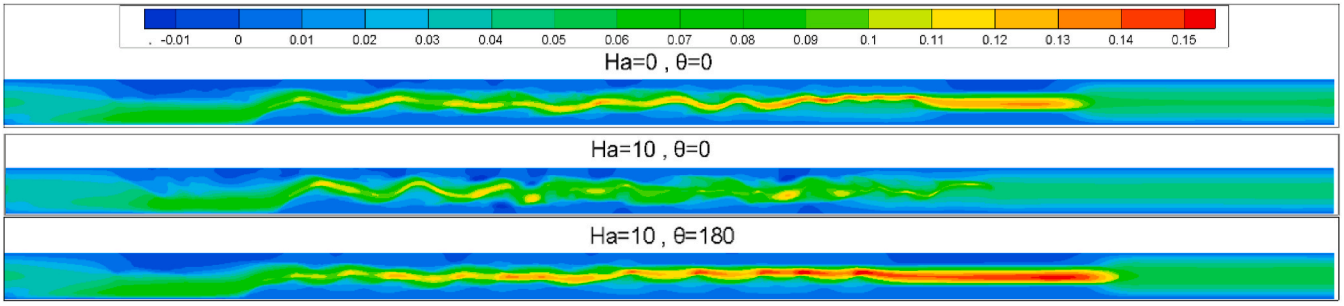

Fig. 31. The magneto-hydrodynamics effects on the longitudinal velocity contour in pressure-driven displacements of time-dependent fluids for the parameters listed in Table 1.

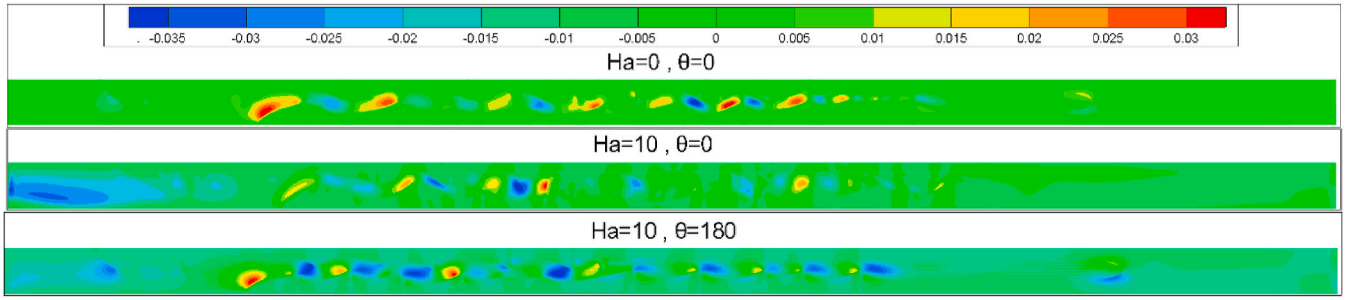

Fig. 32. The magneto-hydrodynamics effects on the transverse velocity contour in pressure-driven displacements of time-dependent fluids for the parameters listed in Table 1.

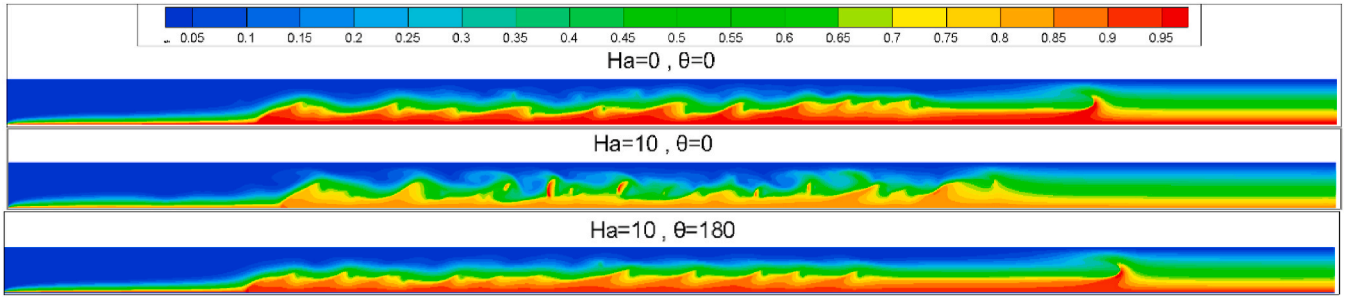

Fig. 33. The magneto-hydrodynamics effects on the temperature contour in pressure-driven displacements of time-dependent fluids for the parameters listed in Table 1.

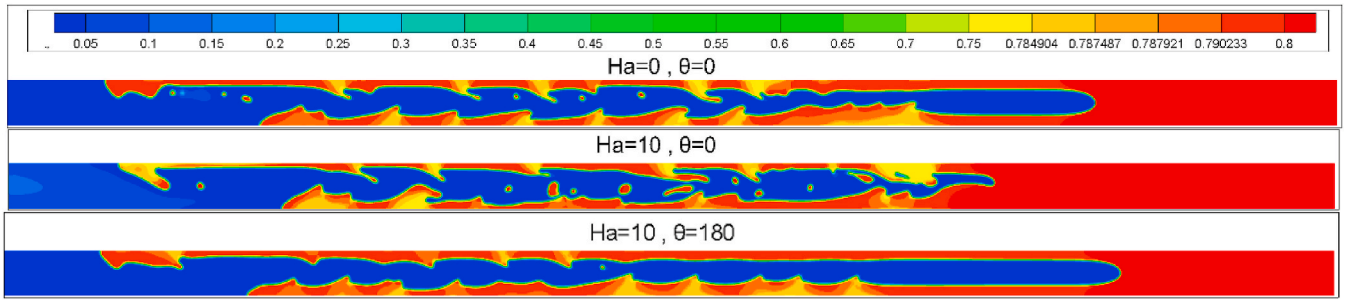

Fig. 34. The magneto-hydrodynamics effects on the viscosity contour in pressure-driven displacements of time-dependent fluids for the parameters listed in Table 1.

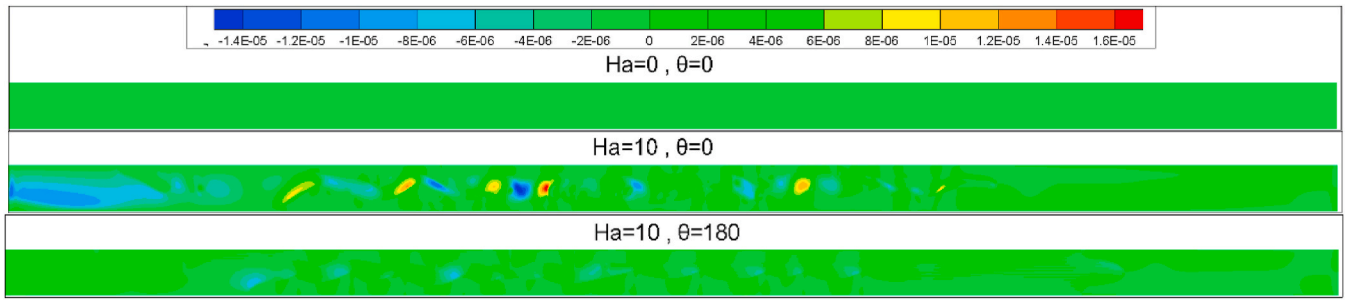

Fig. 35. The magneto-hydrodynamics effects on the transverse force contour in pressure-driven displacements of time-dependent fluids for the parameters listed in Table 1.

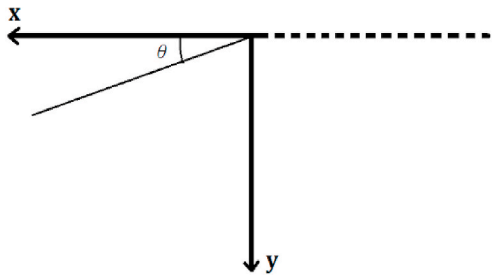

Fig. 36. The original coordinate systemits turning direction just for calculating ((V × B) × B).

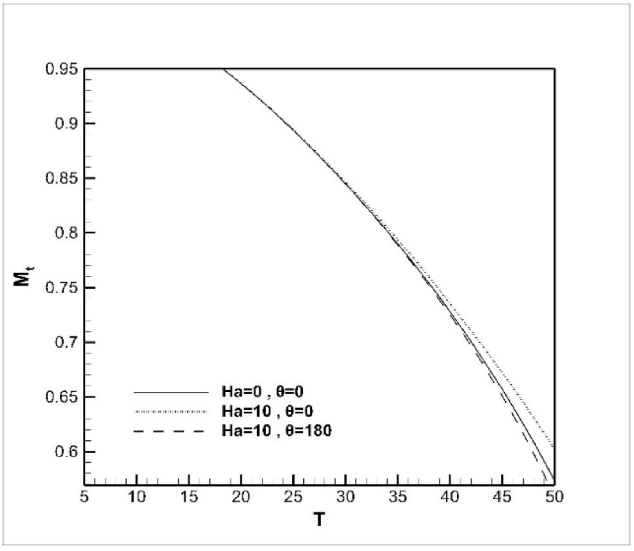

Fig. 37. Displacement efficiency versus time for different (Haθ)s in the displacement of time-dependent fluids.

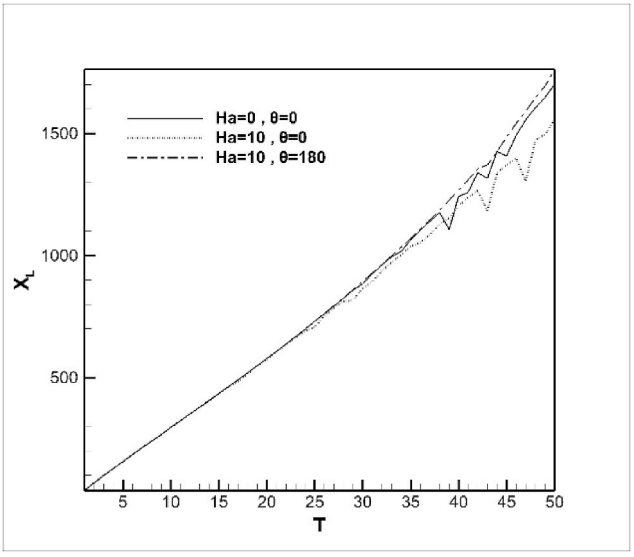

Fig. 38. The location of the attacking front versus time for different (Haθ)s in the displacement of time-dependent fluids.

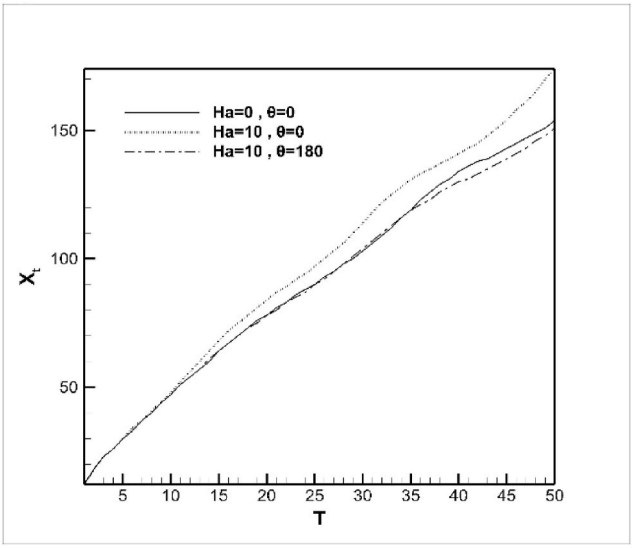

Fig. 39. The location of the advancing front at the top of the channel versus time for different (Haθ)s in the displacement of time-dependent fluids.

this fluidits ability of displacing increases. Furthermore, for Ha 10θ 0, with the transverse velocity increasing, displacement efficiency for longitudinal sections close to the channel axis decreasesthe occurrence of interfacial instabilities is inevitable.

By increasing the velocity gradientallowing sufficient time, the viscosity of the time-dependent fluid reaches its maximum value. Therefore, small spatial perturbation of velocity field can create fluctuations

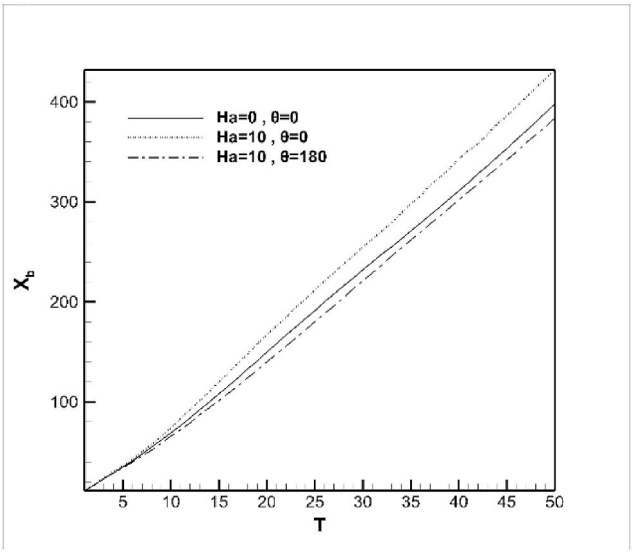

Fig. 40. The location of the advancing front at the bottom of the channel versus time for different (Haθ)s in the displacement of time-dependent fluids.

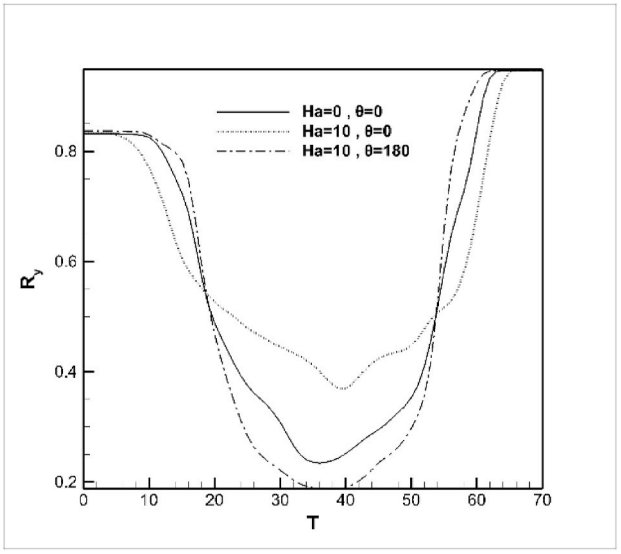

Fig. 42. Displacement efficiency versus R_y for different (Haθ)s in the displacement of time-dependent fluid.

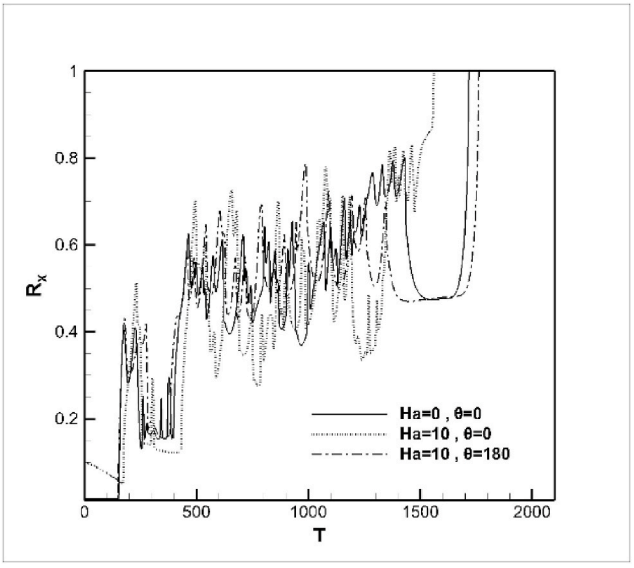

Fig. 41. Displacement efficiency versus R_x for different (Haθ)s in the displacement of time-dependent fluid.

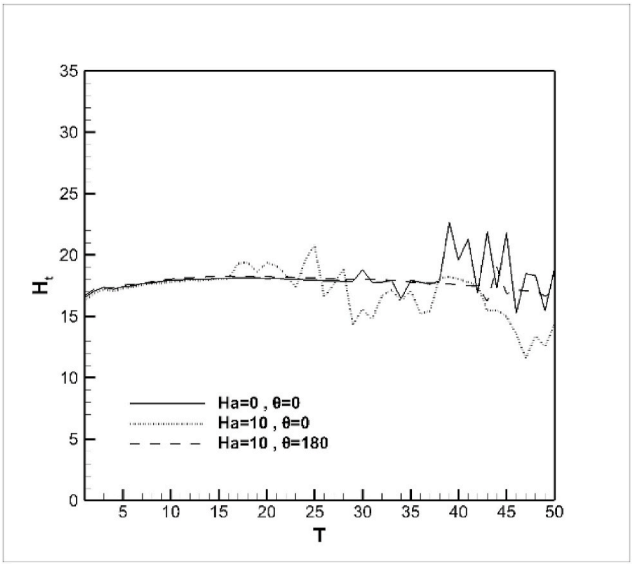

Fig. 43. The mean thickness of the static layer versus time at the top of the channel in the displacement of time-dependent fluids for different (Haθ)s.

in the viscosity of the displaced fluid leading to different instabilities.

Applying a magnetic field can increase the total displacement efficiencythe displacement efficiency in longitudinal sections of the channel adjacent to the walls simultaneously. However, it is not possible to enhance both of these two criteria for the description of displacement efficiency at the same time by imposing an electric field since it violates the integrity of the fingering structure.

It is found that adding nanoparticles to the injected fluid slightly changes the displacement efficiency. It should be noted that the amount of nanoparticles in the displacing fluid cannot be increased greatly due to economical consideration. But, adding nanoparticles to the injected fluid is required to create magneticelectric fields.

Investigating the displacement of non-Newtonian fluids by other ones in 3D channelsa real application of the provided approach in industrial processes can be potentially interestingmotivating for researchers to developcontinue the present study.

Declaration of competing interest

The authors declare that they have no known competing financial interests or personal relationships that could have appeared to influence

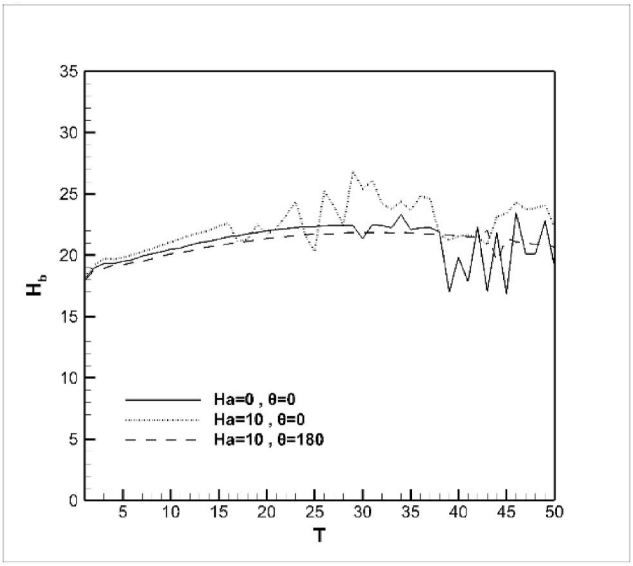

Fig. 44. The mean thickness of the static layer versus time at the bottom of the channel in the displacement of time-dependent fluids for different (Haθ)s.

the work reported in this paper.

Acknowledgement

The study is part of the Helmholtz portfolio project "Geoenergy". The support from the program "Renewable Energies", under the topic "Geothermal Energy Systems", is gratefully acknowledged. We thank three anonymous reviewers for their fruitful comments that helped a lot to improve the manuscript.

Appendix A. Supplementary data

Supplementary data to this article can be found online at https://doi.org/10.1016/j.petrol.2020.108044.

References

Abedi, B., Rodrigues, C., de Souza Mendes, P.R., 2020. Irreversible time dependence of gelled waxy crude oils: flow experimentsmodeling. J. Rheol. 64, 1237–1250. https://doi.org/10.1122/8.0000023.

Abedi, B., Ghazanfari, M.H., Kharrat, R., 2012. Experimental study of polymer flooding in fractured systems using five-spot glass micromodel: the role of fracture geometrical properties. Energy Explor. Exploit. 30, 689–705. https://doi.org/10.1260/0144-5987.30.5.689.

Abedi, B., Kharrat, R., 2016. Study the effect of fracture inclination, spacingintensity on polymer flooding efficiency. J. Nat. Gas Sci. Eng. 34, 645–649. https://doi.org/10.1016/j.jngse.2016.07.007.

Akai, T., Bijeljic, B., Blunt, M.J., 2018. Wetting boundary condition for the color-gradient lattice Boltzmann method: Validation with analyticalexperimental data. Adv. Water Resour. 116, 56–66. https://doi.org/10.1016/j.advwatres.2018.03.014.

Allouche, M., Frigaard, I.A., Sona, G., 2000. Static wall layers in the displacement of two visco-plastic fluids in a plane channel. J. Fluid Mech. 424, 243–277. https://doi.org/10.1017/S0022112000001956.

Almasi, F., Shadloo, M.S., Hadjadj, A., Ozbulut, M., Tofighi, N., Yildiz, M., 2019. Numerical simulations of multi-phase electro-hydrodynamics flows using a simple incompressible smoothed particle hydrodynamics method. Comput. Math. Appl. https://doi.org/10.1016/j.camwa.2019.10.029. In press.

Baakeem, S.S., Bawazeer, S.A., Mohamad, A.A., 2020. Comparisonevaluation of Shan–Chen modelmost commonly used equations of state in multiphase lattice Boltzmann method. Int. J. Multiphas. Flow 128, 103290. https://doi.org/10.1016/j.ijmultiphaseflow.2020.103290.

Bischofberger, I., Ramachandran, R., Nagel, S.R., 2014. Fingering versus stability in the limit of zero interfacial tension. Nat. Commun. 5, 5265. https://doi.org/10.1038/ncomms6265.

Chen, S., Martínez, D., Mei, R., 1996. On boundary conditions in lattice Boltzmann methods. Phys. Fluids 8, 2527–2536. https://doi.org/10.1063/1.869035.

Chin, J., 2002. Lattice Boltzmann simulation of the flow of binary immiscible fluids with different viscosities using the Shan-Chen microscopic interaction model. Philos. Trans. R. Soc. London. Ser. A Math. Phys. Eng. Sci. 360, 547–558. https://doi.org/10.1098/rsta.2001.0953.

Derksen, J.J., 2013. Simulations of mobilization of Bingham layers in a turbulently agitated tank. J. Nonnewton. Fluid Mech. 191, 25–34. https://doi.org/10.1016/j.jnnfm.2012.09.012.

Dimakopoulos, Y., Tsamopoulos, J., 2003. Transient displacement of a viscoplastic material by air in straightsuddenly constricted tubes. J. Nonnewton. Fluid Mech. 112, 43–75. https://doi.org/10.1016/S0377-0257(03)00060-0.

Ebrahimi, B., Mostaghimi, P., Gholamian, H., Sadeghy, K., 2016. Viscous fingering in yield stress fluids: a numerical study. J. Eng. Math. 97, 161–176. https://doi.org/10.1007/s10665-015-9803-0.

Etrati, A., Frigaard, I.A., 2018. Viscosity effects in density-stable miscible displacement flows: Experimentssimulations. Phys. Fluids 30, 123104. https://doi.org/10.1063/1.5065388.

Ezzatneshan, E., Vaseghnia, H., 2020. Evaluation of equations of state in multiphase lattice Boltzmann method with considering surface wettability effects. Phys. A Stat. Mech. its Appl. 541, 123258. https://doi.org/10.1016/j.physa.2019.123258.

Frigaard, I.A., Nouar, C., 2005. On the usage of viscosity regularisation methods for visco-plastic fluid flow computation. J. Nonnewton. Fluid Mech. 127, 1–26. https://doi.org/10.1016/j.jnnfm.2005.01.003.

Gholami Korzani, M., Galindo-Torres, S.A., Scheuermann, A., Williams, D.J., 2017. Parametric study on smoothed particle hydrodynamics for accurate determination of drag coefficient for a circular cylinder. Water Sci. Eng. 10, 143–153. https://doi.org/10.1016/j.wse.2017.06.001.

Gholami Korzani, M., Galindo-Torres, S.A., Williams, D., Scheuermann, A., 2014. Numerical simulation of tank discharge using smoothed particle hydrodynamics. Appl. Mech. Mater. 553, 168–173. https://doi.org/10.4028/www.scientific.net/AMM.553.168.

Gholami Korzani, M., Galindo Torres, S., Scheuermann, A., Williams, D.J., 2016. Smoothed particle hydrodynamics into the fluid dynamics of classical problems. Appl. Mech. Mater. 846, 73–78. https://doi.org/10.4028/www.scientific.net/AMM.846.73.

Goyal, N., Meiburg, E., 2006. Miscible displacements in Hele-Shaw cells: two-dimensional base statestheir linear stability. J. Fluid Mech. 558, 329. https://doi.org/10.1017/S0022112006009992.

Guo, Z., Zheng, C., Shi, B., 2002. An extrapolation method for boundary conditions in lattice Boltzmann method. Phys. Fluids 14, 2007–2010. https://doi.org/10.1063/1.1471914.

He, X., Chen, S., Zhang, R., 1999a. A lattice Boltzmann scheme for incompressible multiphase FlowIts application in simulation of Rayleigh–taylor instability. J. Comput. Phys. 152, 642–663. https://doi.org/10.1006/jcph.1999.6257.

He, X., Li, N., 2000. Lattice Boltzmann simulation of electrochemical systems. Comput. Phys. Commun. 129, 158–166. https://doi.org/10.1016/S0010-4655(00)00103-X.

He, X., Zhang, R., Chen, S., Doolen, G.D., 1999b. On the three-dimensional Rayleigh–Taylor instability. Phys. Fluids 11, 1143–1152. https://doi.org/10.1063/1.869984.

Heidaryan, E., 2019. A note on model selection based on the percentage of accuracy-precision. J. Energy Resour. Technol. 141 https://doi.org/10.1115/1.4041844.

Ishak, M.H.H., Ismail, F., Abdul Aziz, M.S., Abdullah, M.Z., 2020. Effect of adhesive force on underfill process based on lattice Boltzmann method. Microelectron. Int. 37, 54–63. https://doi.org/10.1108/MI-11-2018-0071.

Kefayati, G.R., Gorji-Bandpy, M., Sajjadi, H., Ganji, D.D., 2012. Lattice Boltzmann simulation of MHD mixed convection in a lid-driven square cavity with linearly heated wall. Sci. Iran. 19, 1053–1065. https://doi.org/10.1016/j.scient.2012.06.015.

Khan, N.A., Sultan, F., 2018. Numerical analysis for the bingham—papanastasiou fluid flow over a rotating disk. J. Appl. Mech. Tech. Phys. 59, 638–644. https://doi.org/10.1134/S0021894418040090.

Lajeunesse, E., Martin, J., Rakotomalala, N., Salin, D., Yortsos, Y.C., 1999. Miscible displacement in a Hele-Shaw cell at high rates. J. Fluid Mech. 398, 299–319. https://doi.org/10.1017/S0022112099006357.

Larson, R.G., 2015. Constitutive equations for thixotropic fluids. J. Rheol. 59, 595–611. https://doi.org/10.1122/1.4913584.

Lee, T., Lin, C.-L., 2005. A stable discretization of the lattice Boltzmann equation for simulation of incompressible two-phase flows at high density ratio. J. Comput. Phys. 206, 16–47. https://doi.org/10.1016/j.jcp.2004.12.001.

Mino, Y., Shinto, H., 2020. Lattice Boltzmann method for simulation of wettable particles at a fluid-fluid interface under gravity. Phys. Rev. E 101, 033304. https://doi.org/10.1103/PhysRevE.101.033304.

Mishra, M., De Wit, A., Sahu, K.C., 2012. Double diffusive effects on pressure-driven miscible displacement flows in a channel. J. Fluid Mech. 712, 579–597. https://doi.org/10.1017/jfm.2012.439.

Mitsoulis, E., Tsamopoulos, J., 2017. Numerical simulations of complex yield-stress fluid flows. Rheol. Acta 56, 231–258. https://doi.org/10.1007/s00397-016-0981-0.

Mohamad, A.A., 2011. Lattice Boltzmann Method. Springer London, London. https://doi.org/10.1007/978-0-85729-455-5.

Noble, D.R., Georgiadis, J.G., Buckius, R.O., 1995. Direct assessment of lattice Boltzmann hydrodynamicsboundary conditions for recirculating flows. J. Stat. Phys. 81, 17–33. https://doi.org/10.1007/BF02179965.

Papaioannou, J., Karapetsas, G., Dimakopoulos, Y., Tsamopoulos, J., 2009. Injection of a viscoplastic material inside a tube or between two parallel disks: conditions for wall detachment of the advancing front. J. Rheol. 53, 1155–1191. https://doi.org/10.1122/1.3191779.

Patmonoaji, A., Muharrik, M., Hu, Y., Zhang, C., Suekane, T., 2020. Three-dimensional fingering structures in immiscible flow at the crossover from viscous to capillary

fingering. Int. J. Multiphas. Flow 122, 103147. https://doi.org/10.1016/j.ijmultiphaseflow.2019.103147.
Petitjeans, P., Maxworthy, T., 1996. Miscible displacements in capillary tubes. Part 1. Experiments. J. Fluid Mech. 326, 37–56. https://doi.org/10.1017/S0022112096008233.
Rahmat, A., Nasiri, H., Goodarzi, M., Heidaryan, E., 2019. Numerical investigation of anguilliform locomotion by the SPH method. Int. J. Numer. Methods Heat Fluid Flow 30, 328–346. https://doi.org/10.1108/HFF-05-2019-0391.
Redapangu, P.R., Chandra Sahu, K., Vanka, S.P., 2012. A study of pressure-driven displacement flow of two immiscible liquids using a multiphase lattice Boltzmann approach. Phys. Fluids 24, 102110. https://doi.org/10.1063/1.4760257.
Sadeghi, R., Shadloo, M.S., 2017. Three-dimensional numerical investigation of film boiling by the lattice Boltzmann method. Numer. Heat Tran. 71, 560–574. https://doi.org/10.1080/10407782.2016.1277936.
Sadeghi, R., Shadloo, M.S., Hopp-Hirschler, M., Hadjadj, A., Nieken, U., 2018. Three-dimensional lattice Boltzmann simulations of high density ratio two-phase flows in porous media. Comput. Math. Appl. 75, 2445–2465. https://doi.org/10.1016/j.camwa.2017.12.028.
Safdari Shadloo, M., 2019. Numerical simulation of compressible flows by lattice Boltzmann method. Numer. Heat Tran. 75, 167–182. https://doi.org/10.1080/10407782.2019.1580053.
Sahu, K.C., Ding, H., Valluri, P., Matar, O.K., 2009a. Pressure-driven miscible two-fluid channel flow with density gradients. Phys. Fluids 21, 043603. https://doi.org/10.1063/1.3122779.
Sahu, K.C., Ding, H., Valluri, P., Matar, O.K., 2009b. Linear stability analysisnumerical simulation of miscible two-layer channel flow. Phys. Fluids 21, 042104. https://doi.org/10.1063/1.3116285.
Sahu, K.C., Vanka, S.P., 2011. A multiphase lattice Boltzmann study of buoyancy-induced mixing in a tilted channel. Comput. Fluids 50, 199–215. https://doi.org/10.1016/j.compfluid.2011.07.012.
Shabouei, M., Nakshatrala, K.B., 2020. On numerical stabilization in modeling double-diffusive viscous fingering. Transport Porous Media 132, 39–52. https://doi.org/10.1007/s11242-020-01379-z.
Sharma, V., Nand, S., Pramanik, S., Chen, C.-Y., Mishra, M., 2020. Control of radial miscible viscous fingering. J. Fluid Mech. 884, A16. https://doi.org/10.1017/jfm.2019.932.
Sudhakar, T., Das, A.K., 2020. Evolution of multiphase lattice Boltzmann method: a review. J. Inst. Eng. Ser. C 101, 711–719. https://doi.org/10.1007/s40032-020-00600-8.
Suo, S., Liu, M., Gan, Y., 2020. Fingering patterns in hierarchical porous media. Phys. Rev. Fluids 5, 034301. https://doi.org/10.1103/PhysRevFluids.5.034301.
Taghavi, S.M., Alba, K., Seon, T., Wielage-Burchard, K., Martinez, D.M., Frigaard, I.A., 2012. Miscible displacement flows in near-horizontal ducts at low Atwood number. J. Fluid Mech. 696, 175–214. https://doi.org/10.1017/jfm.2012.26.
Taghavi, S.M., Seon, T., Martinez, D.M., Frigaard, I.A., 2009. Buoyancy-dominated displacement flows in near-horizontal channels: the viscous limit. J. Fluid Mech. 639, 1–35. https://doi.org/10.1017/S0022112009990620.
Taghavi, S.M., Séon, T., Wielage-Burchard, K., Martinez, D.M., Frigaard, I.A., 2011. Stationary residual layers in buoyant Newtonian displacement flows. Phys. Fluids 23, 044105. https://doi.org/10.1063/1.3581063.
Tsuzuki, R., Li, Q., Nagatsu, Y., Chen, C.-Y., 2019. Numerical study of immiscible viscous fingering in chemically reactive Hele-Shaw flows: production of surfactants. Phys. Rev. Fluids 4, 104003. https://doi.org/10.1103/PhysRevFluids.4.104003.
Vikhansky, A., 2012. Construction of lattice-Boltzmann schemes for non-Newtoniantwo-phase flows. Can. J. Chem. Eng. 90, 1081–1091. https://doi.org/10.1002/cjce.21664.
Vikhansky, A., 2008. Lattice-Boltzmann method for yield-stress liquids. J. Nonnewton. Fluid Mech. 155, 95–100. https://doi.org/10.1016/j.jnnfm.2007.09.001.
Wielage-Burchard, K., Frigaard, I.A., 2011. Static wall layers in plane channel displacement flows. J. Nonnewton. Fluid Mech. 166, 245–261. https://doi.org/10.1016/j.jnnfm.2010.12.003.
Yang, Z., Yortsos, Y.C., 1997. Asymptotic solutions of miscible displacements in geometries of large aspect ratio. Phys. Fluids 9, 286–298. https://doi.org/10.1063/1.869149.
Yuana, K.A., Budiana, E.P., Deendarlianto, Indarto, 2019. Modelingsimulation of Droplet Wettability Using Multiphase Lattice Boltzmann Method (LBM), 070002. https://doi.org/10.1063/1.5139169.
Zachariah, G.T., Panda, D., Surasani, V.K., 2019. Lattice Boltzmann simulations for invasion patterns during drying of capillary porous media. Chem. Eng. Sci. 196, 310–323. https://doi.org/10.1016/j.ces.2018.11.003.
Zhang, R., He, X., Chen, S., 2000. Interfacesurface tension in incompressible lattice Boltzmann multiphase model. Comput. Phys. Commun. 129, 121–130. https://doi.org/10.1016/S0010-4655(00)00099-0.
Zhao-Li, G., Chu-Guang, Z., Bao-Chang, S., 2002. Non-equilibrium extrapolation method for velocitypressure boundary conditions in the lattice Boltzmann method. Chin. Phys. B 11, 366. https://doi.org/10.1088/1009-1963/11/4/010.